GROWTH OF NANOWIRES ON GAAS (100) SUBSTRATE

GROWTH OF NANOWIRES ON GAAS (100) SUBSTRATE

BY

SUBIR CHANDRA GHOSH, M.SC

A thesis
Submitted to the School of Graduate Studies
in Partial Fulfillment of the Requirements
for the Degree
Doctor of Philosophy

McMaster University

DOCTOR OF PHILOSOPHY (2009)   McMaster University

Department of Engineering Physics   Hamilton, Ontario

TITLE: Growth of Nanowires on GaAs (100) Substrate

AUTHOR: Subir Chandra Ghosh, M.Sc (AIT, Thailand)

SUPERVISORS: Dr. Ray R. LaPierre and Dr. Peter Kruse

NUMBER OF PAGES: XVII, 116

Abstract

Using gold as seed particles, the vapour-liquid-solid (VLS) growth of GaAs nanowires by molecular beam epitaxy on GaAs (100) substrates was investigated with a view to understanding and controlling the growth directions of nanowires. The crystallographic orientation as well as surface density of nanowires was found to be significantly affected by surface topography resulting from surface preparation prior to nanowire growth. Elongated pits of varying dimensions and orientation were formed on GaAs (100) substrates depending on the interaction of GaAs with gold or surface oxide. An in-depth analysis was carried out regarding the formation of pits as well as chemical composition of the oxide layer during the seed particle formation process.

By analyzing the orientation-dependent structural properties of nanowires at different stages of growth, the origin of multi-directionality of nanowires on GaAs (100) substrates has been explored, and it has been shown that the growth directionality of nanowires can be significantly triggered to either the <011> or <111> direction by optimizing the growth rate as well as size of seed particles. Crystallographic properties of nanowires have also been discussed with reference to their growth directions.

Acknowledgement

I would like to take this opportunity to express my profound gratitude to my supervisors Dr. Ray LaPierre and Dr. Peter Kruse for their encouragement, support, and guidance throughout this project. I am also grateful to my supervisory committee members Dr. Adrian Kitai and Dr. Gianluigi Botton, who generously took the effort of reviewing my work on a time-to-time basis, and provided me invaluable advice.

I wish to express my gratitude to Dr. Dmitri Malakhov, Dept. of Materials Science and Engineering, who provided me invaluable suggestions and references to understand the thermodynamic aspects related to nanowire growth.

I am indebted to Dr. Brad Robinson for his assistance with growths in MBE, and also numerous scintillating discussions pertaining to various aspects of thin-film growth. Special thanks go to CEDT personnel: Doris, Zhilin, Graham, Linda for their help and assistance throughout this project. I can not imagine carrying out this research without the facilities available at Canadian Center for Electron Microscopy (CCEM). Many thanks go to Glynis, Fred, Carmen, Steve, Julia, Christian, and Andy who were always accessible for help in any form – from sample preparation to training, and characterization. I am also thankful to the administrative staffs of Engineering Physics: Marilyn, Fran, Lori, Samantha for making my life easier in many instances.

I would like to acknowledge Mark Biesinger, Surface Science Western, University of Western Ontario, for assistance and helpful discussion related to the XPS analysis. I also wish to thank Dr. Nadi Braidy for help in TEM, and Dr. Todd Simpson

for his help with thin-foil preparation for TEM analysis. I am also grateful to my friends and colleagues who my made my life easier and enjoyable during my study.

Finally, I find no word to express my feelings towards my family who shared my vision and did enormous sacrifices to make this journey possible. This thesis would have been impossible without their unconditional support and inspiration.

to my father

Table of Contents

List of Figures

List of Tables

Chapter 1

Introduction

The last decade has witnessed tremendous research attention in the field of nanowires due to their potential for fabricating nanoscale devices and systems for a wide range of applications. The growth of one-dimensional structures called 'whiskers' was first reported in the 1960s, but the renewed interest in recent times primarily stems from the effort to find an alternative route of device fabrication that will allow feature sizes which are not possible with existing techniques due to technological and physical limitations. This impetus is corroborated by size-induced novel properties, different from the bulk, making nanowires an interesting avenue of research.

Nanowires have a unique geometry with a length much larger than their diameter. The diameter is in the range of tens of nanometers and the length much longer, typically a few micrometers. This increased surface-to-volume ratio provides extremely high sensitivity to the changes in surface conditions, and can be used as sensing probes for the implementation of biological and chemical sensors [1, 2] . Moreover, this property can be instrumental for the realization of highly efficient solar cells [3, 4].

Nanowire-based p-n junctions [5, 6], field effect transistors [7], optoelectronic devices such as light- emitting diodes (LEDs) [8, 9] and lasers [10] have already been demonstrated. Another significant application, often overlooked, is its use as thermoelectric materials. The efficiency of a thermoelectric device is measured in terms of a figure of merit, ZT, which is defined as $ZT = \sigma S^2 T/\kappa$, where σ is the electrical conductivity, κ is the thermal conductivity, S is the Seebeck coefficient and T is the temperature. These parameters are interdependent – optimizing one parameter adversely affects others without any significant gain in ZT. Recently, it has been experimentally demonstrated that the thermal conductivity (κ) of nanowires is significantly lower than the bulk counterpart (while keeping σ and S unchanged) [11, 12]. This result is very promising for the implementation of highly efficient thermoelectric devices.

Like other nanostructures, nanowires can be fabricated either by the 'top-down' method, the dominant industrial technique, in which bulk material is carved to nanometric structures using lithographic techniques, or by the 'bottom-up' approach in which atoms are self-assembled to create larger structures through controlled crystallization of materials from liquid or vapour sources. The 'top-down' method, limited by lithographic ability, involves tedious microfabrication processes that pose difficulty in maintaining the uniformity and chemical composition on the nanoscale. On the other hand, the bottom-up method not only offers the ability to create nanoscale structures of very small dimension, but also allows changes in chemical composition during growth, which is not achievable with standard top-down methods. Nanowires can be fabricated with source material supplied either from the vapour phase or solution

phase using different techniques that have been covered in detail in the literature [13]. Growth of nanowires has been carried out extensively by using vapour phase synthesis with a number of techniques such as laser ablation, chemical vapour deposition, or molecular beam epitaxy. Nanowires are predominantly grown by the vapour-liquid-solid (VLS) mechanism in which growth materials are supplied in the 'vapour' phase, and a 'liquid' metal particle, acting as catalyst, promotes the growth of solid crystalline materials by precipitation under the metal particle. In addition to promoting the 1-D growth, metal particles also determine the size and position of the nanowires on the substrate.

1.1 Vapour-Liquid-Solid Growth

The growth of one dimensional structures called 'whiskers' was first demonstrated by Wagner and Ellis [14] in 1961 by using gold as an 'impurity' particle in the VLS mechanism. Understanding of this process was enriched by the contribution from Givargizov [15] in the mid-70s, and later in the early 90s by Hiruma et al. [16, 17] who extended it to the growth of GaAs nanowires and demonstrated the formation of p-n junctions in GaAs nanowires. The latter finding was also a demonstration of a simplistic method of growing 1-D nanocrystals, which, in essence, made an explosion of interest in nanowires all over the world.

The core principle of the VLS mechanism is the introduction of a liquid-solid interface in vapour phase growth. An 'impurity', usually a metal particle, is utilized to form a liquid alloy with the material from a substrate or with material supplied in the

vapour phase. If growth material is supplied at a constant temperature above the eutectic point, the 'impurity' particles will at first reach their thermodynamic equilibrium at growth temperature and then eventually become supersaturated with the growth material which, in effect, acts a driving force for nucleation under the particle, and growth takes place by precipitation at the solid-liquid interface, as illustrated in Figure 1. The particle is not consumed and essentially remains unchanged during growth, thus serving as a 'catalyst' during growth.

In VLS growth, the major requirement is that the metal particle must form a liquid alloy to create a supersaturation that will act as a driving force for the crystallization of nanowire material. If the material forms a eutectic with the metal particle, the supersaturaton can be achieved by raising the temperature above the eutectic point while supplying the growth material in the vapour phase. Selection of the catalyst and optimization of the growth conditions can be simplified by considering the binary phase diagram of the growth material of interest and the metal particle.
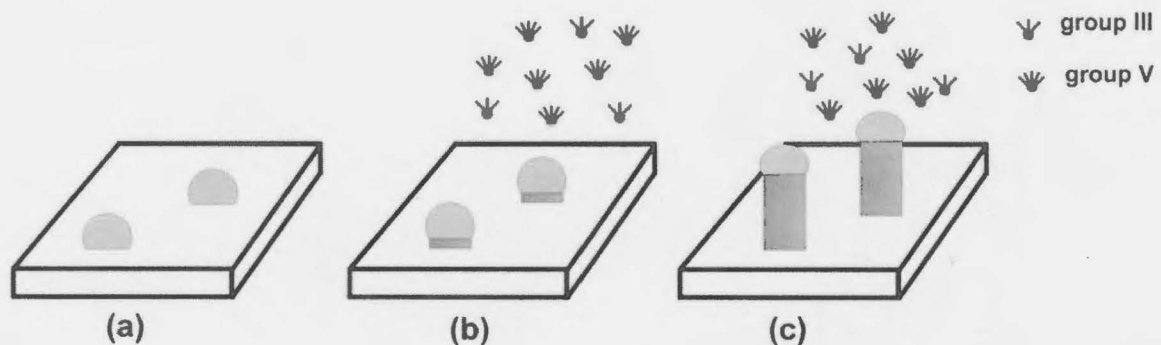
Figure 1.1 Illustration of the vapour-liquid-solid mechanism (a) Formation of gold particles on the substrate. (b) The nanowire growth is initiated after growth material is supplied. (c) The nanowire becomes longer as the growth is continued.

Another requirement for the VLS mechanism to operate, according to Wagner and Ellis, is that the liquid solution must be stable, which, in essence, imposes a limit to the minimum diameter achievable of the liquid particle and the wire. The stability of a liquid droplet of curvature 'r' surrounded by a vapour of the same material depends on the degree of supersaturation and is given by the Gibbs-Thomson law:

$$r_{min} = \frac{2\sigma_{LV}\Omega_L}{kT \ln \sigma}$$
        Eq. 1.1

where σ_{Lv} is the liquid-vapour interfacial energy, Ω_L is the atomic volume of growth species in the liquid, k_B is Boltzmann's constant, T is the absolute temperature and σ is the degree of supersaturation, defined as $\sigma = (p - p_0)/p_0$ in which p is the vapour pressure and p_0 is the equilibrium vapour pressure of the growth material at the growth temperature.

The VLS mechanism has become the dominant method for fabricating nanowires for a rich variety of materials – such as elemental semiconductors, III-V semiconductors, II-VI semiconductors, oxides and nitrides.

1.1.1 Role of 'Impurity' Particle

Wagner et al.[18] emphasized the requirement of a solution-forming agent or 'impurity' for the VLS growth of 1-D structures, which, in heterogeneous reactions, was assumed to act as a catalyst and also to provide an 'enhanced accommodation coefficient' that results in a long lifetime of the adsorbed gas molecules at the liquid surface.

As generally defined, a catalyst is known to accelerate a chemical reaction by lowering the activation barrier to reaction - it forms bonds with the reacting molecules, and allows them to react to a product, and detaches from the product to make it available for the next reaction [19]. A catalyst thus significantly changes the kinetics of a chemical reaction and makes the reaction rate much faster. If the metal particle acted as a catalyst during nanowire growth, it must decrease the activation barrier for the decomposition of precursor species and induce a locally increased concentration of growth material that eventually precipitates, leading to the 1D growth. The catalytic activity of the metal particle is still a question of open debate – for growth systems where precursor decomposition is required for growth, activation energy for the growth of nanowires, as calculated by Wagner et al. [18] and later by other groups [20-22], is the same as that for the planar growth without gold. Quite contrary to that, there are also reports [20, 23, 24] that support the catalytic activity of the metal particle during nanowire growth. On the other hand, in techniques like molecular beam epitaxy (MBE), growth materials are directed as elemental beams to the growth surface, which essentially precludes catalytic activity of the metal particle during growth. In such a case, the metal particle can be considered to act as a collector [25] of materials which facilitates the growth in one direction. The latter definition does not conform to the generally accepted definition of catalysis, as described at the beginning of this section, which is mostly used to describe chemical reactions. If the latter phenomenon is defined as chemical catalysis, the role of the particle can be termed as a 'physical catalyst' during nanowire growth. However, due to process-dependent functionality of metal particles and ambiguity in experimental data

regarding the role of particles, metal particles participating in the VLS are commonly termed as 'seed particles' in the literature. In order to keep abreast with present literature, we will use the same term throughout the thesis. In any case, particle-assisted nanowire growth is the dominant growth process because of its simple reproducibility and application to an enormous variety of growth methods and materials. It allows tuning of the size and density of nanowires by controlling the distribution of metal particles before growth.

Ni [26], Cu [27, 28], Al [29] and Fe [30] have been used as seed particles for the growth of nanowires, but Au outperforms other metals in producing oriented and size selected nanowires. The reasons for this are not clearly understood, but the properties that make gold a better candidate are probably due to its chemical stability (inertness) and formation of low eutectic alloys with many semiconductors of interest [31].

1.2 Nanowire Growth Direction

As observed by Wagner and Ellis [18], whiskers grow along the <111> direction as (111) layers perpendicular to the solid-liquid interface. This means that, depending on the substrate orientation, the topographical distribution of nanowires will also change. For cubic crystals like Si or GaAs, the <111> direction corresponds to the orthogonal appearance of nanowires on (111) substrates and an inclination of 35.3° with (100) substrates. From a crystallographic point of view, there exist four equivalent <111> directions, separated azimuthally by 90° from each other on (100) surfaces. This means that nanowires can grow along these four equivalent directions [32]. While true for non-

polar substrates (such as Si), on polar substrates such as GaAs (100), nanowires are found to preferentially nucleate from As-faced (B-faced) planes [33] in comparison to Ga-faced (A-faced) planes. As a result, nanowires on GaAs (100) substrates grow along two equivalent <111> directions, separated azimuthally by 180°. As they grow from B-faced planes, these directions are commonly referred to as <111> B directions.
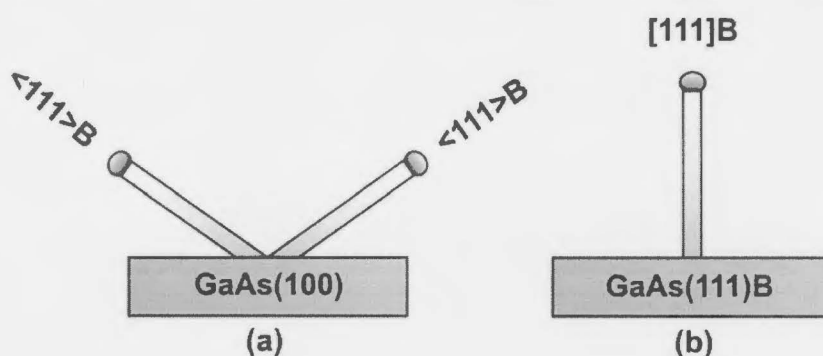
Figure 1.2. Schematic illustrating the energetically preferable <111>B directions of nanowires on different substrate orientations: (a) inclined at 35.3° on a GaAs (100) substrate and (b) orthogonal to a GaAs (111)B substrate.

1.3 Background of Present Work

(111) substrate orientations are generally preferred due to the orthogonal growth direction of nanowires that gives better control as well as understanding of the growth process. However, nanowires growing along this direction contain periodic arrays of stacking faults perpendicular to the growth direction, which could have an adverse effect in the physical properties of the nanowire [34]. The defect density can be suppressed by optimizing the growth conditions [35, 36], but getting a completely defect-free nanowire along the <111> direction is still elusive. On the other hand, (100) orientated substrates, used for industrial applications, offer the advantage of (i) a wide range of growth

conditions which result in good epitaxial layer quality, (ii) well developed processing technology and (iii) natural cleavage planes normal to the (100) orientation. To take advantage of this existing technology as well as facilitate integration of nanowires with thin film devices, it is necessary to understand and control their growth on this substrate orientation.

As mentioned earlier, nanowires preferably grow along the <111> direction which is inclined at 35.3° on (100) substrates. In addition to growing along energetically favourable directions, GaAs nanowires, grown by MBE, have been reported to grow along <111>A and <110> directions due to strain. Moreover, <110> directed nanowires have been claimed to be defect-free [33]. On the other hand, the presence of defect-free <100> directed InP nanowires grown on InP(001) substrate by metal organic vapour phase epitaxy (MOVPE) have also been reported [34]. It therefore appears that there exists a possibility of growing defect-free nanowires on (100) substrates.

Nanowire growth direction has been found to be influenced by the diameter (d) of the seed particle [37]. Taking energetics into consideration, Schmidt *et al* [38] demonstrated that for large diameters, the growth direction with lowest seed particle-nanowire interface energy is dominant, whereas for small diameters the surface energy of the nanowire determines the preferential growth direction. It has also been shown that nanowires can change their growth direction from <111> to <110> at a crossover diameter of approximately 20 nm; i.e., nanowires having a diameter less than 20 nm grew along the <110> direction. However, this model cannot explain the presence of relatively large (~50nm) <100> oriented nanowires on (100) substrates [34], since surface energy

varies as (100) > (110) > (111) [39]. On the other hand, Wu *et al* [40] calculated the relative abundance of nanowires based on growth directions and presented a somewhat different picture – (i) for d<10 nm, 98% of nanowires grew along the <110> direction; (ii) for 10<d<20 nm, 65% grew along the <112>, 20% along the <110> and 15% along the <111> direction and (iii) for d>20nm, 65% grew along <111>, 30% along <112> and 5% along the <110> direction. These findings are not consistent with other reports and drawing any conclusion regarding the growth directions of nanowires is difficult. Moreover, scant attention has been given to understanding and controlling the growth of GaAs nanowires on GaAs (100) substrates, especially in growth techniques like MBE.

The purpose of this present work was to explore and to understand the origin of growth directionality as well as structural properties of GaAs nanowires grown on GaAs (100) substrates by molecular beam epitaxy (MBE) and hence, to optimize the growth conditions with a view to triggering the growth in a specific direction while minimizing stacking faults.

1.4 Thesis Overview

The growth and characterization techniques are reviewed in Chapter 2. It introduces a methodology for substrate preparation required prior to growing nanowires and discusses different characterization techniques, with an emphasis given to issues pertinent to nanoparticle and nanowire characterization.

Gold nanoparticles stand as the cornerstone of metal catalyzed growth of 1D nanocrystals and it necessitates an understanding about the formation of these particles on

GaAs (100) substrates. As reported earlier [41], monodisperse gold particles with a narrow size distribution can be fabricated on UV-Ozone oxidized GaAs substrates by annealing a thin layer of gold. In order to understand the formation of these particles, a systematic approach was adopted that is the subject of discussion in Chapter 3 and 4, and previously published in the Journal of Applied Physics [42, 43]. In Chapter 3, an in-depth study regarding the chemical composition of UV-Ozone oxide as well as its changes as a result of formation of gold particles has been analyzed by X-ray photoelectron spectroscopy. Chapter 4 provides a deeper insight into the chemistry and physics of the common engineering practice of using a proximity cap, while annealing compound semiconductors such as GaAs. The role of different caps during annealing together with the change in chemical composition of the oxide as well as surface topography of GaAs (100) substrates has been discussed.

The influence of GaAs (100) substrate preparation on Au-catalyzed GaAs nanowires, published in Nanotechnology [44], is discussed in Chapter 5. By growing nanowires on GaAs (100) substrates subjected to different surface preparations, it has been shown that the density and orientation of nanowires are influenced by the evolving topography prior to growth. Onset of nucleation of nanowires has also been discussed.

In Chapter 6, we discuss the ways of controlling the growth direction of nanowires on GaAs (100) substrates by tailoring the growth rate and particle size. Structural properties of nanowires based on their orientation have also been discussed.

Chapter 2

Experimental Methods

This chapter provides a brief overview of the experimental methods used throughout this thesis – from surface preparation to analysis of nanowires. Emphasis has been given to discuss the issues pertaining to the research of nanostructures.

2.1 Sample Preparation Prior to Nanowire Growth

As mentioned in section 1.0, nanowire growth in the VLS mechanism is mediated by the presence of seed particles which, apart from promoting the crystal growth, also determine the size and position of the nanowires. In order to achieve a uniform distribution of nanowires, it is required to ensure a uniform distribution of monodisperse seed nanoparticles prior to the growth of nanowires.

Gold is preferably used as the seed particles for the growth of nanowires. There are different routes of forming gold nanoparticles on the substrate - colloidal gold by wet chemistry [45, 46], patterning gold by electron beam lithography [47], deposition of gold

through pre-patterned masks (such as alumina) [48], aerosol deposition [49, 50] or by galvanic displacement mediated by di-block copolymers [49]. These processes have their relative advantages and disadvantages. For example, aerosol deposition is size selective, but carbon contamination is a major problem [51]. Uniform distribution of gold can be formed using e-beam lithography (EBL), but it is a slow as well as costly process for mass production. Use of di-block copolymers allows control of the distance between the particles, but post-processing and removal of carbon from the substrate is problematic. The most convenient and commonly used technique is the deposition of a layer of gold which is annealed at high temperature prior to growth to form nanoparticles having a size distribution primarily determined by the initial thickness of the gold layer.

Epi-ready n-type GaAs (100) wafers (Source: Wafer Technology Ltd.) with a carrier concentration of $(1-5) \times 10^{18}$ cm^{-3} were used as substrate material throughout this thesis. These were processed in an UVOCS UV/ozone reactor to remove hydrocarbon contamination. In addition, this process leads to the growth of an oxide layer, in particular for III-V semiconductors [52, 53].

UV-ozone oxidation involves two wavelengths of which the shorter one (184.9 nm) is associated with the generation of ozone, whereas the longer wavelength (253.7 nm) supplies energy in the oxidation process. The active species is assumed to be atomic oxygen which is formed photo-chemically above the surface and must travel into the bulk until it cleaves a gallium-arsenic bond. For the case of atomic oxygen reacting with bare GaAs (100) surfaces [54], it was found that oxygen atoms displace arsenic atoms to form gallium oxide as the initial and also thermodynamically favored product [55]. Molecular

oxygen has a similar effect, however with a much lower reaction probability [56, 57]. Molecular oxygen may result from recombination of two oxygen atoms during their diffusion into the bulk GaAs. However, this reaction pathway is expected to make a minor contribution to GaAs oxidation. With increasing oxygen exposure, arsenic oxides are also formed until complete oxidation of gallium and arsenic species is achieved. As a result of the diffusion process, the thickness of the oxide layer follows a logarithmic dependence on UV-Ozonation time [53] and after 20 minutes of processing in the UVOCS reactor, an oxide layer of 3.5 nm was found to grow on GaAs (100) substrates.

Substrates were loaded into the e-beam evaporation system where a gold film of either 1 nm or 4 nm thickness was deposited at room temperature (base pressure $<10^{-8}$ Torr) at an average rate of 0.1 nm/sec as monitored by a quartz crystal monitor. In some cases, the gold was deposited directly on the Epi-ready wafer, or after etching the oxide with 10% buffered HF followed by a rinse in de-ionized water for 10 minutes. For the analysis of gold particles, annealing was carried out in a N_2 environment using an AG Associates Mini-Pulse rapid thermal annealing (RTA) furnace at typical ramp rates of 1 °C/sec. The density and distribution of gold nanoparticles or islands is dependent, as we reported earlier, on surface processing as well as initial thickness of the gold layer [41]. However, to reduce the loss of arsenic during annealing, a GaAs proximity cap, an additional piece of GaAs wafer placed face-to-face with the substrate, was used in all cases. A detailed study, as discussed in Chapter 4, will show that the use of proximity caps is insignificant for cases where the annealing is carried out at 500°C for the formation of gold nanoparticles.
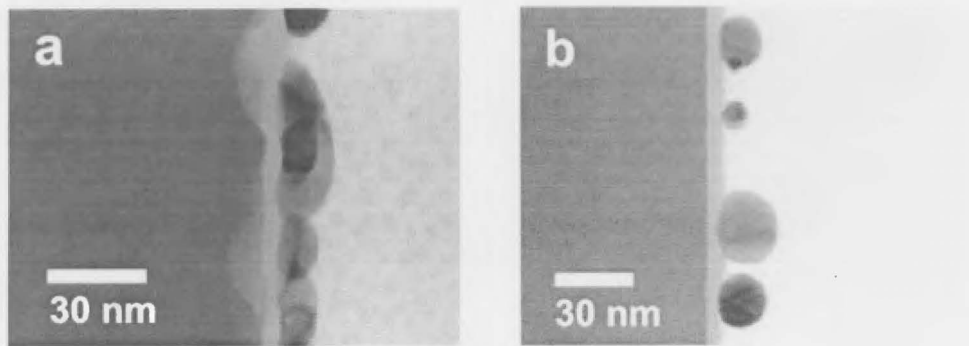
Figure 2.1. Formation of gold particles on UV-Ozone oxidized (a) GaAs (100) and (b) GaAs (111)B substrates after annealing 4 nm of gold at 500 °C for five minutes.

The work, presented in this thesis, is focused on understanding the growth directionality of nanowires on GaAs (100) substrates. However, at the very beginning of the project, a series of studies involving both GaAs (100) and GaAs(111)B oriented substrates were carried out regarding the formation of gold particles and evolution of surface topography as a result of processing steps like UV-Ozone oxidation and annealing. The preliminary work has not been included in the thesis except the key result in Figure 2.1, which shows the formation of gold nanoparticles on oxidized substrates. It is clear from these cross-sectional TEM images that GaAs (100) substrates are severely roughened by the formation of long range pits, whereas the topography of GaAs(111)B remains unaffected.

2.1.1 Molecular Beam Epitaxy

Epitaxy refers to the arrangement of deposited atoms on a substrate and allows the growth of high-quality layers of the same or related crystal structure as the substrate. Molecular beam epitaxy (MBE) is carried out in ultra-high vacuum where beams of atoms or molecules are directed towards the substrate which is held at a temperature suitable for the growth of that particular material. In MBE, the flux rate is made sufficiently slow such that the mean free path of the atoms or molecules is longer than the source-to-substrate distance to ensure a 'molecular beam' for growth, meaning there are no collisions between the atoms or molecules of the beam. The flux of incoming atoms can be controlled by using a mechanical shutter[1] to grow a film to an accuracy of a single monolayer which allows the creation of sharp interfaces or abrupt doping profiles.

The MBE system used for the growth of nanowires was a gas source molecular beam epitaxy (GSMBE) system in which group III materials (Ga, In) are supplied as elemental beams, effusing from a solid source by evaporation, and group V materials are supplied from a gas source (AsH_3, PH_3) which is cracked at high temperature before entering the chamber. The resulting As species, after cracking, is a mixture of monomers, dimers and tetramers; the relative abundance of these species depends on the temperature, pressure and the degree to which thermodynamic equilibrium is achieved in the cracker cell. Due to the low incorporation probability (sticking coefficient) of tetramers into the growing crystal, the cell (in our system) is maintained at a temperature of 950 °C to ensure a predominance of dimers – for instance, the As_2/As_4 beam flux ratio is expected

---

[1] The response time of the shutter is less than 0.1s, which is considerably less than the time required (typically 1-5 s) to grow a monolayer.

to be on the order of 10^4, As_2/As about 10^2, As_2/AsH about 10^5, and As_2/H about 10^2 [58]. Hydrogen is therefore always present during growth, but does not incorporate in the crystal under normal growth conditions.

The unique feature of MBE is the ability to monitor in-situ growth using electron beams without interrupting the growth process. Our system is equipped with reflection high energy electron diffraction (RHEED) to monitor the structure of the outermost layers of the sample surface before and during the growth. It is also equipped with infra-red pyrometry for absolute temperature measurement, and a hydrogen inductively coupled plasma (ICP) system to desorb the oxide before starting the growth. The atomic hydrogen, produced by cracking H_2, reacts with the oxide and removes it at a lower temperature (480 °C) in comparison to thermal desorption which is generally carried out at higher temperature (>600 °C) [59]. Moreover, cleaning the surface by hydrogen plasma does not roughen the surface by severe pitting that occurs during the thermal cleaning process. However, there is evidence of short length scale roughening associated with hydrogen cleaning [60]. Hydrogen cleaning is also capable of removing carbon (not as efficiently as oxide), and it does not remove silicon dioxide [61].

Each GaAs (100) wafer was cleaved into four quarters and mounted, after processing and metallization as described in section 2.1, onto a holder in dust-free conditions under a high efficiency particulate air (HEPA) filter. The holder, made of a molybdenum puck, was machined in such a way that the quarter pieces fit into a recessed ledge of the puck and did not move laterally during sample transfer.
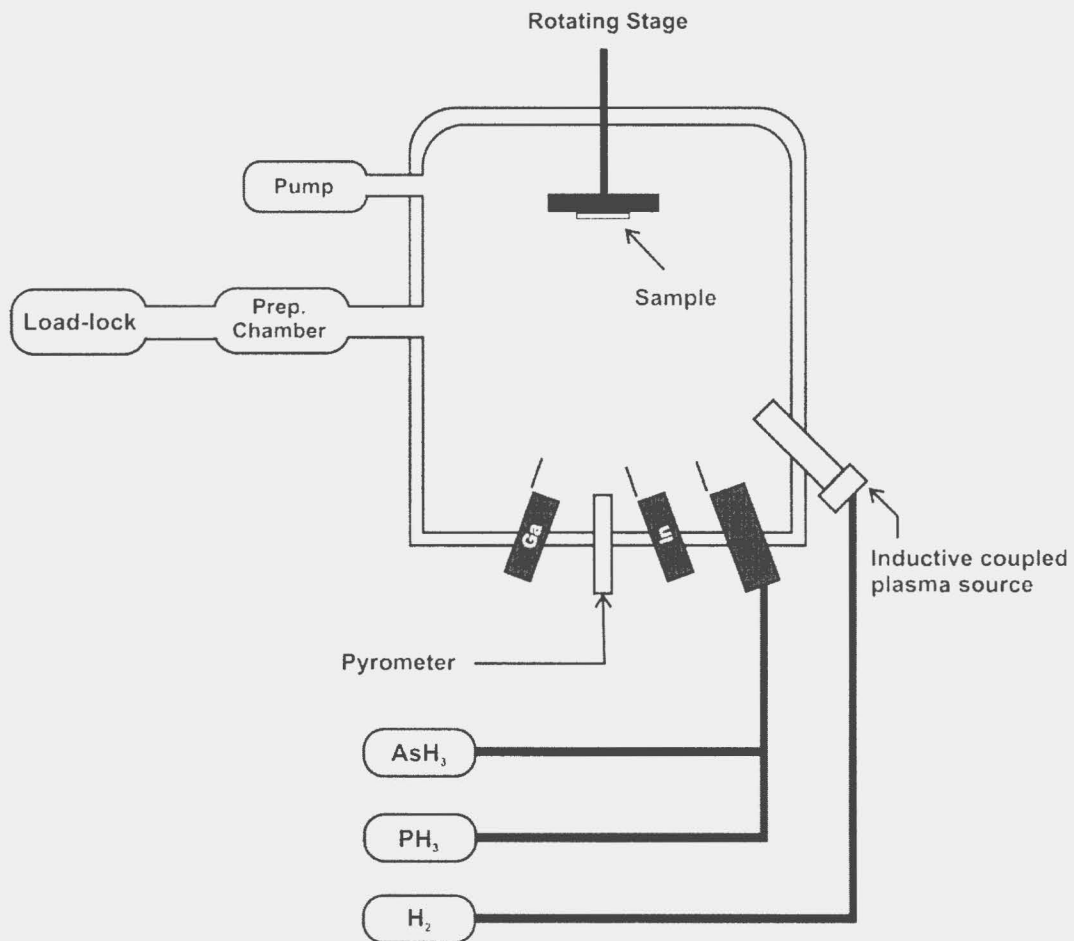
Figure 2.2. Simplified schematic of the gas source molecular beam epitaxy system used to grow nanowires in this thesis.

The sample was inserted into the load-lock and after pumping down to a desired level, the sample was moved into a preparation chamber where it was degassed at 300 °C for 15 minutes. After degassing, the sample was transferred to the main chamber where it was oriented face-down for exposure to the beams inside the chamber. The sample was rotated at a rate of one revolution per 4.5s to ensure structural homogeneity during growth.

Prior to starting the growth, any residual oxide was desorbed by ICP plasma at 480 °C for 10 mins under excess arsenic pressure. The substrate was then elevated to the desired growth temperature and after stabilization of As_2 flux, the Ga shutter was opened to initiate the growth of nanowires. After the growth was completed, the Ga shutter was closed and the sample was cooled down under excess As_2 pressure which was completely turned off at 350 °C.

2.2 Characterization Techniques

In this thesis, we are primarily interested in the structural properties of nanowires which include topographical and morphological features, compositional analysis as well as crystallographic information (such as crystal structure, defects, and growth direction). Compositional analysis was carried out by X-ray photoelectron spectroscopy (XPS) and a suite of analytical tools available in the transmission electron microscope (TEM), such as energy-dispersive X-ray spectroscopy (EDXS) and electron energy loss spectroscopy (EELS). Topographical and morphological data was primarily collected by using scanning electron microscopy (SEM), whereas crystallographic information was obtained from the analysis of nanowires by TEM. Given the abundance of literature regarding all these techniques, we will not resort to detailed discussions. We will rather focus on fundamental concepts with emphasis given to describing the experimental conditions optimized for the studies presented in this thesis.

2.2.1 X-ray Photoelectron Spectroscopy

X-ray photoelectron spectroscopy, abbreviated as XPS, involves the bombardment of a material *in-vacuo* by soft monochromatic X-rays to eject electrons by photo-ionization. The core-level electrons emanating from the material have an energy that is indicative of the chemical state of the parent atom, with a kinetic energy given by the following equation:

$$E_k = h\nu - E_B - \phi_{sp}$$ Eq. 2.1

where E_k is the kinetic energy of the emitted atom, $h\nu$ is the energy of exciting X-ray photons, E_B is the binding energy of the electron and ϕ_{sp} is the work function of the spectrometer. Since the electron binding energy is the parameter of interest, the spectrometer is usually set up to record the spectrum in terms of binding energy, rather than on the measured kinetic energy scale. Electrons contributing to the spectrum come within 10 nm from the surface, making XPS a surface-sensitive technique.

The standard notation attributed to a peak is written in terms of different quantum numbers, similar to describing an electron in an atom - nl_j where, n is the principal quantum number, l is the orbital angular momentum quantum number, j is the total angular momentum quantum number, and $j = l + s$ where s is the spin angular momentum quantum number ($\pm 1/2$). Of the four subshells, the s level is called the singlet and all other levels ($l > 0$) give rise to doublets due to spin-orbit coupling – for instance, $3d_{3/2}$ and $3d_{5/2}$. The peaks corresponding to the components of the doublets

have an energy difference which is proportional to the spin-orbit coupling constant, and their relative intensities are given by the ratio of their degeneracy $(2j+1)$, as shown in Table 2.1.

Table 2.1. XPS peaks and their relative intensities due to spin orbit coupling

Subshell	j values	Area ratio
s	$1/2$	-
p	$1/2, 3/2$	$1:2$
d	$3/2, 5/2$	$2:3$
f	$5/2, 7/2$	$3:4$

The intensity of a peak is directly proportional to the density of the atoms in the sampled volume. For a homogeneous solid, the relative atomic concentration of a chosen element A is given by the following equation:

$$C_A = \frac{I_A/S_A}{\sum_n (I_n/S_n)} \qquad \text{Eq. 2.2}$$

where C_A is usually expressed as atomic percent, I_A and I_n correspond to the intensity from element A and summed intensities for all the elements respectively. S_A and S_n refer to the corresponding relative sensitivity factors (RSF). The value of RSF is dependent on the photoemission cross-section of the core level and varies by a factor of 100 (excluding Li and Be) across the periodic table.

For our analysis, we used the XPS set-up available at Surface Science Western at the University of Western Ontario. Each sample was analyzed by using a Kratos AXIS Ultra X-ray photoelectron spectrometer employing a monochromatic Al K_α X-ray source

(1486.71 eV) and charge neutralizer system. The instrument work function was calibrated

to give a binding energy (BE) of 83.96 eV for the Au $4f_{7/2}$ line for metallic gold, and the

spectrometer dispersion was adjusted to give a BE of 932.62 eV for the Cu $2p_{3/2}$ line of

metallic copper. Survey scans and high resolution analyses were carried out in an area

300 μm x 700 μm in size, with pass energies of 160 eV and 20 eV and step sizes of 0.7

eV and 0.1 eV, respectively. Relative atomic concentration was calculated from the

intensities of the major photoelectron spectral lines (integrated areas) by subtracting a

Shirley background using the software CASA XPS. All the XPS work was carried out

with the help of Mark Biesinger at Surface Science Western at the University of Western

Ontario, London, Ontario.

2.2.2 Electron Microscopy

The fundamental concept in electron microscopy is to make use of electron-matter

interactions by taking advantages of very small wavelengths, resulting from wave particle

duality, associated with highly energetic electrons. Electron microscopes can be broadly

divided into two groups – scanning electron microscopes and transmission electron

microscopes. Both can provide images with high spatial resolution although they are

fundamentally different in terms of operating principles. Scanning electron microscopes

rely on emission of secondary or back-scattered electrons to reproduce the topographical

image. On the other hand, TEM, as the name implies, utilizes the modulated

wavefunction of the transmitted electrons (change in amplitude, phase) through thin

specimens to produce a diffraction pattern in the back focal plane or an image in the

object plane. However, electron microscopes are also equipped with different analytical tools that make them very powerful and versatile techniques for characterization.

2.2.2.1 SEM Analysis

In this thesis, a JEOL 7000F SEM was employed for topographical imaging of gold nanoparticles as well as nanowires by using secondary electrons. Specimens were mounted on flat stubs with carbon tape and tiny amounts of silver paste at two corners to minimize charging effects. For cross-sectional imaging, specimens were mounted on 'angled stubs' and tilted in-situ inside the SEM chamber until the specimen becomes parallel to the electron beam. Gold nanoparticles, as small as 4 nm, were imaged with high energy electron beams (15 kV) at a low working distance (4 mm). Nanowires, relatively larger than particles, were imaged with medium energy electrons (10 kV) and larger working distance (6/10 mm) in order to provide enough space for tilting between the stub and the pole piece. It is important to note here that it is better to take a plan-view image of nanowires before tilting the specimen. This is especially true for nanowires on (100) substrates that grow in different crystallographic directions; i.e., at various angles with the substrate.

In combination with imaging, the tilting and rotating capability of the samples within the SEM was used to measure the angle subtended by a nanowire with the substrate. It is better to find an area with a special feature, easily distinguishable from the surroundings, in order to keep track of the area during tilting. As shown in Figure 2.3, the specimen was then tilted until the nanowire of interest (or a sub-set of nanowires)

appeared as spots, i.e., parallel to the beam direction. The tilting angle (α) was then

subtracted from 90° to find the angle of inclination of the nanowires with the substrate.

The angle of inclination was then assigned to the corresponding crystallographic

direction by reference to the wafer flats provided by the manufacturer. The angle was

determined by using the following equation:

$$\cos\theta = \frac{a \cdot b}{|a\|b|}$$

Eq. 2.3

where a and b Miller indices for the wafer (100) and the nanowire direction.
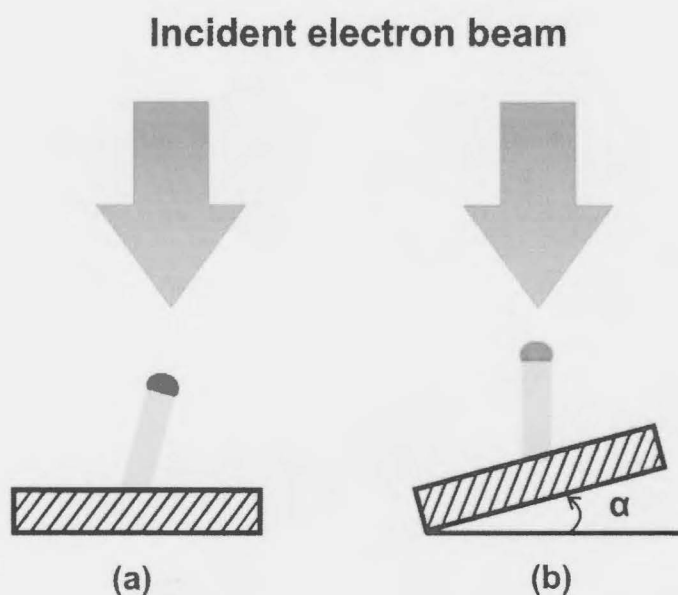
Figure 2.3. Calculation of the angle of inclination of nanowires with the substrate using SEM. The initial specimen (a) was tilted (b) until the nanowire appeared as dots in the image; i.e., perpendicular to the beam direction.

Using the above equation, the angle, for example, between (100) and (111) planes can be calculated as:

$$\theta = \cos^{-1}\left(\frac{(100)}{\sqrt{1+0+0}}\frac{(111)}{\sqrt{1+1+1}}\right) = 54.7° \qquad \text{Eq. 2.4}$$

This means that the <111> direction, perpendicular to the (111) plane, will subtend an angle of $(90° - 54.7°) = 35.3°$ with respect to the (100) substrate surface. The tilting angle (α) represents the angular separation between the (100) plane and the plane perpendicular to the growth direction of nanowires, and it can be used to determine the crystallographic orientation of nanowires simply by calculating the angular separation of different planes with respect to the substrate, as shown in Figure 2.4.
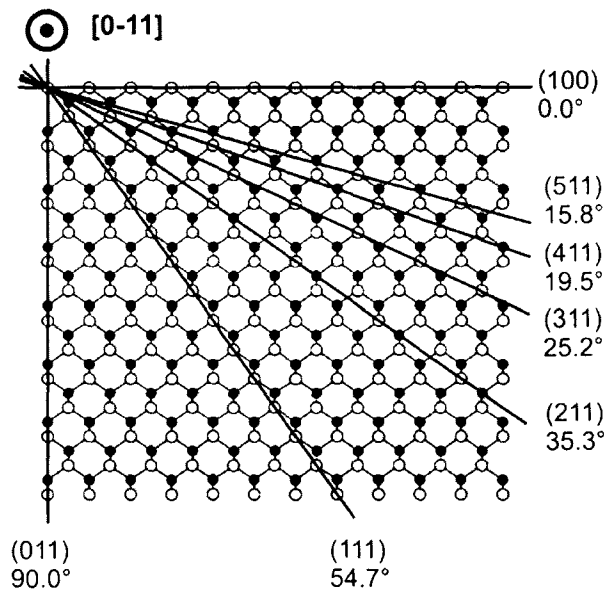
Figure 2.4. 2-D illustration of the major crystal planes and their angular separation with respect to (100) planes in a zincblende crystal structure, as viewed along the [0-11] direction (adapted from [39]).

Figure 2.4 shows the angular relationships between major crystallographic orientations and the (100) plane and it also represents a simplistic approach to estimate the surface energy by counting the areal density of bonds penetrating the planes of respective orientations. As calculated by Braun *et al* [39], the surface energy corresponding to different planes shows a $\cos\theta$ dependence, where θ is the angle of the plane with respect to the (100) plane. This approach takes energetics into consideration and provides a simplified way of assigning preferred crystallographic directions to nanowire growth based on their angle of inclination with the substrate.

2.2.2.2 TEM Analysis

For analysis by TEM, the foremost requirement is to ensure that the sample is 'thin' enough for the transmission of electrons while minimizing the absorption and scattering within the specimen. Preparing the 'thin foil', hereafter called the TEM sample, is the key for collecting and interpreting reliable data from the specimen. For studying gold nanoparticles and smaller nanowires (growth times less than 3 mins), cross-sectional TEM samples were prepared by mechanical polishing followed by dimpling and ion-milling. To prepare cross-sectional samples, two pieces of the specimen (about 2 mm width and 8-10 mm length) are glued together with equal number of Si "dummy" bars (usually 3 bars) on each side. It was then mechanically polished to a thickness less then 200 μm. A circular piece of 3mm was then cut by using an ultrasonic cutter and it was later dimpled with a Fischione precision dimpling system. The sample was then loaded into the ion-miller where the TEM sample was bombarded with low-energy (4 kV) inert Ar gas ions at low angle ($\leq 4°$) until a hole appeared in the middle of the sample. The ion milling system is equipped with a monitoring system that allows visualization of the on-going progression of the milling process. However, preparing a TEM sample in this conventional way is a tedious and time consuming process. Note that one has to be very careful (patient as well!) during preparation and handling as the foil gets thinner.

Plan-view samples were prepared for the analysis of spatial distribution of gold nanoparticles/clusters. Preparation of plan-view samples was rather easy and less time consuming. A piece (3 mm diameter) of the specimen is cut and polished, and

27

subsequently dimpled and milled from the back side to expose a thinner area around the hole for analysis.

For TEM analysis, long nanowires can be separated from the substrate by sonication in solution (acetone or water) and transferred onto a holey carbon TEM grid by placement of a few drops of the solution [62]. If the nanowires grow along different directions, as in the case of GaAs (100), it is not possible to distinguish among different nanowire growth direction after sonication. To study the growth-dependent structural properties, nanowires of interest were selectively removed from the substrate by using a focused ion beam in the SEM system (FIB-SEM). The advantage of this technique is that an area of interest can be selected using the high resolution imaging capability of SEM, and a thin- foil of the specific area of interest can be prepared. In our case, the nanowire of interest was selected first and an area (approximately $1\mu m$ by $5\mu m$) surrounding the nanowire was in-situ coated with carbon or platinum to protect the feature during the subsequent milling process. The surrounding substrate was then removed from the longer sides in such a way that 'wedge like' shapes met at the bottom leaving a thin piece of material (lamella[2]). The tip of a nanomanipulator was positioned on top of the lamella and attached to the sample by injecting carbon between the tip and the lamella. The lamella cut was then completed, lifted off and transferred to a patterned copper grid sitting on a stub. The tip of the nanomanipulator was cut off, and the lamella attached to the copper grid was then thinned down by using the Ga ion beam until it became electron transparent. The chamber was then vented and the thin foil (TEM sample) was then taken

---

[2] Note that the term 'lamella' is used to mean a thin piece of material lifted off from the substrate by milling. It will be referred to as the TEM sample.

out for analysis. FIB-SEM systems available at McMaster University (Zeiss NVision 40) and at the University of Western Ontario (LEO 1540XB) were used for preparing TEM samples.

All the TEM samples were first checked with a Philips CM12 conventional TEM operating at 120 keV. For cross-sectional samples, images were usually taken under two-beam conditions in bright field mode and plan-view samples were analyzed in the zone axis condition. Note that the imaging condition should be carefully noted for interpretation of the image.

Given the small feature size in our sample, a high resolution field emission microscope, a JEOL JEM-2010F, operating at 200 keV was often employed. Lattice resolved images were analyzed using Digital Micrograph software, developed by Gatan, to determine the crystallographic direction and crystal structure of the specimens. However, this microscope can also run in the scanning mode in which a converged beam is allowed to scan on the specimen and the intensity of the transmitted beam is recorded as a function of position. This mode of operation is generally known as scanning TEM (STEM), which in addition to imaging, is used in analytical characterization by utilizing inelastic scattering processes.

2.2.2.3 Analytical TEM

As a result of inelastic processes, energetic electrons may dislodge inner shell electrons. If the resulting electron vacancy is filled by an electron from higher energy levels, x-ray photons are emitted having energy equal to the difference in the energy between upper and lower levels. The emitted X-ray, known as a characteristic X-ray, is unique to the ionized atom and as a result, the elements in the periodic table exhibit different sets of characteristic X-ray lines. In Energy Dispersive X-ray Spectroscopy (EDXS), the number of characteristic X-rays is recorded as a function of energy and a spectrum is generated.

The JEOL JEM-2010F is equipped with a Si(Li) ultrathin polymer (Moxtek™ AP3.3, active area 30 mm^2 with solid angle 0.114 sr) window energy dispersive detector supplied by Oxford instruments. The spectrometer is controlled by software (INCA) which is also used for acquisition and analysis of the spectrum. The SiteLock™ was always enabled to correct for any drift during the acquisition of the spectrum. Spectral data was taken along a line of interest (line scan) or from a point of interest (point scan). In some cases, elemental mapping was generated from an area of interest, and the data was analyzed to calculate the elemental distribution at any point, or across a line of interest. Apart from producing an elemental map of a given area, the latter technique gives the flexibility of post-processing to retrieve elemental data anywhere in the mapped area.

EDXS analysis is straightforward, and it is preferably carried out for elemental quantification although the accuracy is rarely better than 10% [63]. This accuracy further

deteriorates in the case of lighter elements (Z<10) due to absorption of low energy x-ray photons in the specimen. Moreover, specimen drift and X-ray fluorescence becomes an important issue for elemental quantification especially for nanoparticles embedded on the substrate. The latter problems can be eliminated by using spectroscopic techniques such as Electron Energy Loss Spectroscopy (EELS) in TEM. In this technique, loss of energy of the incident electrons after undergoing core-shell ionization is measured with the help of a high resolution (~1 eV) spectrometer and the characteristic edge of the element is displayed in a spectrum. It allows standardless[3] quantification which can detect smaller amounts of an element compared to EDXS [64, 65] . This technique works extremely well if the energy loss is within 100-1000 eV and has become a method of choice for the quantification of lighter elements, some transition metals and rare earth elements. For heavier elements, such as Ga/As, due to high energy loss, the edge is not sharp which makes the quantification rather complex. In this thesis, EELS was employed for the detection of Ga to complement the data obtained from other techniques.

---

[3] For accurate elemental quantification, EDXS requires the analysis of a standard sample of known composition as the specimen.

Chapter 3

Analysis of Gold Particles on UV-Ozone Oxidized GaAs (100) Substrates

This section presents a thorough X-ray photoelectron spectroscopic study regarding the composition of UV-Ozone oxide films formed on GaAs (100) as well as the impact of annealing at 500 °C for the purpose of gold nanoparticle formation, which has been published in the Journal of Applied Physics [42]. The UV-ozone oxide has been found to consist of oxides of gallium and arsenic in addition to having a significant contribution from elemental arsenic concentrated mostly at the substrate-oxide interface. An intermediate suboxide species, $-As_xGa_2O$, is found to make up a substantial part of the oxide layer, mostly near the surface region, whereas the interface to bulk GaAs is dominated by Ga_2O_3. As_2O_3 is found to be the dominant oxide in the initial UV-ozone oxide layer, while the oxide layer becomes rich in Ga_2O_3 as the sample is annealed at 500 °C for 300 s in a dry N_2 environment. It is also found that gold does not alloy with Ga

during the formation of gold nanoparticles due to separation of gold from the substrate by the UV-ozone oxide layer.

3.1 Experimental Details

Epi-ready n-type GaAs (100) wafers (Source: Wafer Technology Ltd.) with a carrier concentration of $(1-5) \times 10^{18}$ cm^{-3} were used as substrate material. These were processed in a UVOCS UV/ozone reactor in order to remove hydrocarbon contamination and to produce an oxide layer with a desired thickness as a function of oxidation time. UV-ozone oxidation for 20 minutes produced about 3.5 nm of oxide thickness. A gold film of 1 nm thickness was deposited on the UV-ozone oxidized samples at room temperature using an e-beam evaporation system (base pressure better than 10^{-8} Torr) at an average rate of 0.1 nm/sec, as monitored by a quartz crystal monitor. Annealing was carried out at 500 °C for 300 s in a N_2 environment using an AG Associates Mini-Pulse rapid thermal annealing (RTA) furnace at a typical ramp rate of 1 °C/sec. To reduce the loss of arsenic during annealing, a GaAs proximity cap, an additional piece of GaAs wafer placed face-to-face with the substrate, was used in all cases.

The following samples were prepared and analyzed for this study: (a) GaAs with an oxide layer of 3.5 nm (20 min UV-ozone treatment) before and after annealing, (b) GaAs with a 3.5 nm oxide layer and a 1nm Au layer before and after annealing, and (c) two GaAs samples UV-ozone oxidized for 10 and 50 mins which produces an oxide thickness of 2.5 nm and 4.5 nm respectively [66]. 1 nm Au films were deposited on these oxides and annealed at 500°C for a duration of 300s before subjecting them to XPS

study. Four reference samples were also prepared for XPS analysis: (a) For the GaAs standard sample, a GaAs substrate was sputter etched with a 4 kV argon ion beam for 20 minutes prior to analysis; (b) For the As metal sample, an As metal lump (99.9999%) ampouled under argon was purchased from Alfa Aesar. It was loaded into the XPS chamber via an argon filled glove box. It was then argon ion sputter etched for 20 minutes to produce a clean, fresh surface; (c) For Ga_2O_3, 99.995% Ga_2O_3 was purchased from Alfa Aesar and analysis was carried out both on an as-received surface and on a sample after cleavage in vacuum; and (d) Gallium metal was obtained from a used time-of-flight secondary ion mass spectrometry (TOF-SIMS) gallium ion gun source and subjected to analysis after sputter etched with argon ions for 1 minute.

Characterization of UV-ozone oxides of GaAs by XPS requires identification of photoelectron peaks with different oxidation states. Accurate energy assignment of these peaks is important in the determination of the various species present on the surface. Although the NIST XPS standard database [67] is a valuable source of reference data, it is limited by the collection of the results as reported by various researchers. For example, there are many entries for 3d lines of Ga and As, but there are few reports available on 2p which is more sensitive to surface properties as it has smaller inelastic mean free path (IMFP) in comparison to 3d or 3p. Even though the 2p peaks have the highest intensities in the XPS spectra, their deconvolution into different species is much less straightforward due to smaller differences in chemical shifts. Nevertheless they are of particular value for obtaining depth-resolved information.

Deconvolution and assignment of XPS peaks to different arsenic species is more accurate and easier than those of Ga because of the larger chemical shifts among the different oxides of arsenic. There is ambiguity and potential for error in the assignment of peaks arising from the Ga components. For example, the peak having a binding energy of 23.2 eV has varyingly been assigned to a chemical state of Ga [68], an 'intrinsic photoemission process' [69] or to O 2s [70]. A peak at 21.6 eV has been assigned to Ga(OH)$_3$ [71, 72] or to a ternary compound like GaAsO$_4$ [68, 69, 73] with a corresponding peak of As 3d at 45.2 eV. However, there is general agreement in the literature about the assignment of the peak at 20.6 eV to Ga$_2$O$_3$ [74-76].
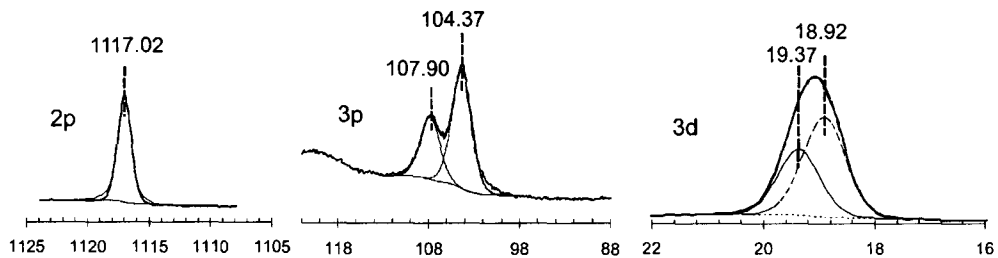
Figure 3.1. XPS spectra of different peaks of gallium obtained from the GaAs standard sample shows the 2p peak of Ga (from GaAs) located at 1117.02 eV. Peaks at 107.90 eV and 104.37 eV correspond to 3p$_{1/2}$ and 3p$_{3/2}$, respectively. Peaks at 19.37 eV and 18.92 eV represent 3d$_{3/2}$ and 3d$_{5/2}$, respectively.

3.2 Results and Discussion

3.2.1 Peak Assignment

In XPS analysis, the peak assignment is critical for correct species identification. This becomes particularly crucial when the change in chemical shift is small for different

oxidation states of an element or when binding energy ranges associated with different components of the system overlap. With this in mind, clean surfaces (see experimental section) of a GaAs substrate, a Ga_2O_3 crystal and samples of elemental Ga and elemental As were subjected to XPS measurements to obtain accurate references. The Ga and As spectra of GaAs are shown in Figure 3.1 and 3.2, respectively. Figures 3.3 and 3.4 show the spectra obtained from elemental arsenic and gallium oxide, respectively.
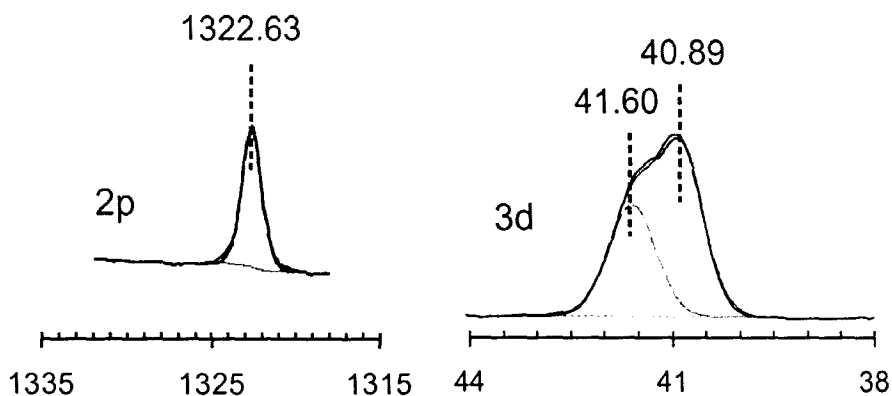
Figure 3.2. XPS spectra from the GaAs standard show the 2p peak of As (from GaAs) located at 1322.63 eV. Peaks at 41.60 eV and 40.89 eV correspond to the $3d_{3/2}$ and $3d_{5/2}$ peaks of As (from GaAs) respectively.

Next, XPS spectra of the UV-ozone oxidized samples were acquired. All spectra were charge corrected to the main line of carbon 1s (C–C and C–H from adventitious carbon) set to 284.80 eV. The gallium 3d spectrum was deconvoluted with four peaks assigned to $Ga(OH)_3$, Ga_2O_3, $–As_xGa_2O$ and GaAs while the arsenic 3d spectrum was fitted with three peaks assigned to elemental As, As_2O_3, and As_2O_5. The 2p spectra of As were fitted with two peaks representing the contributions from arsenic oxide and

36

elemental arsenic. The 2p spectra of Ga were fitted with two peaks assigned to $-As_xGa_2O$

and Ga_2O_3.

1323.29

41.55
42.25

2p   3d

1332   1329   1325   1322   1318   48   46   44   42   40   38
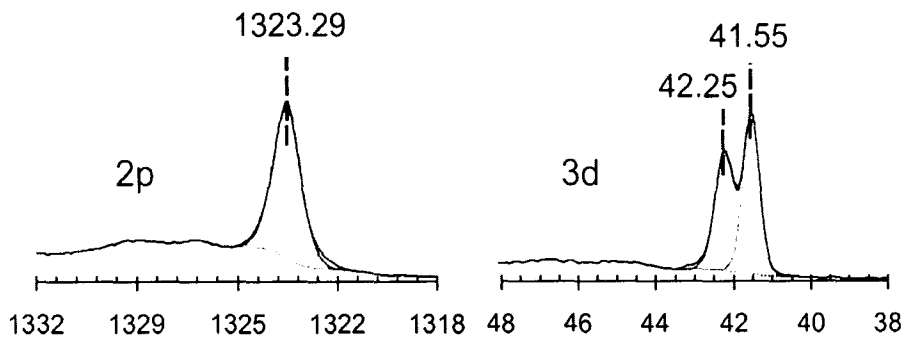
Figure 3.3. 2p and 3d peaks obtained from the elemental As standard. The binding energy associated with 2p is 1323.29 eV. The 3d doublet is positioned at 42.25 eV and 41.55 eV.

1117.70   105.64   20.56
                 109.04   20.11

2p   3p   ┌─ 105.14 *   3d   ┌─ 19.28*
                         └─ 101.74*   └─ 18.84*

1110 1115 1120 1125   125 115 105 95 85   26 24 22 20 18 16
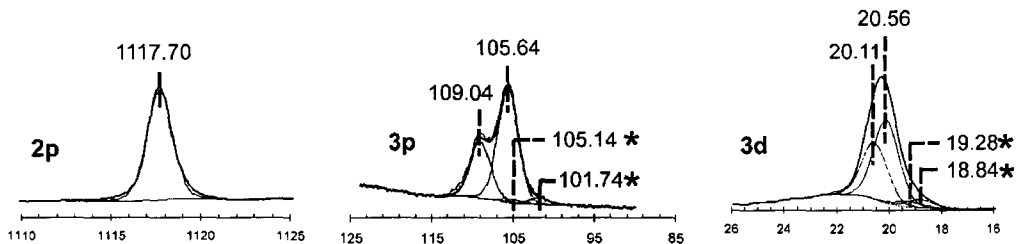
Figure 3.4. XPS spectra from the Ga_2O_3 standard. The 2p peak of Ga (from Ga_2O_3) is located at 1117.70 eV. The 3p doublets of Ga (from Ga_2O_3) are at 105.64 eV and 109.04 eV. The 3d peaks are at 20.11 eV and 20.56 eV. Small amounts of an unidentified impurity (possibly metallic gallium) give rise in the fitting process to a doublet marked "*".

The presence of gallium suboxide in the UV-ozone oxide layer has been reported

previously but no explanation was given regarding the transient formation of gallium in

the +1 oxidation state as opposed to the +3 oxidation state which is present initially in

GaAs and also in the ultimate product Ga_2O_3. Rather, we postulate the presence of an

intermediate species $-As_xGa_2O$ which is formed, as shown in Figure 3.5, by gradual

37

gallium to arsenic bond breaking as increasing amounts of atomic oxygen are inserted throughout the UV-ozone oxidation process. This species is non-stoichiometric as it forms stochastically and gradually as oxygen atoms become available during the UV/ozonation process. Initial displacement of arsenic by atomic oxygen is consistent with experiment [54] and calculations [55] on surface species. While eventually the $-As_x$ part of this species will get oxidized, it will substantially be present in its original GaAs environment (fully bonded to Ga) or as elemental As (partially or not bonded to Ga). In our deconvolution of the arsenic signal (for example in Figure 3.7), we did not distinguish between these arsenic species, because of the small differences in chemical shift.

The depth location of different species can be judged based on the inelastic mean free paths (IMFPs) for different orbitals, and an estimate of this can be made based on the IMFPs for pure GaAs as follows [28]:

As 2p with a kinetic energy of 162 eV, $1\sigma = 0.472$ nm, $3\sigma = 1.28$ nm

Ga 2p with a kinetic energy of 369 eV, $1\sigma = 0.762$ nm, $3\sigma = 2.29$ nm

Ga 3p with a kinetic energy of 1381 eV, $1\sigma = 2.084$ nm, $3\sigma = 6.252$ nm

As 3d with a kinetic energy of 1444 eV, $1\sigma = 2.161$ nm, $3\sigma = 6.48$ nm

Ga 3d with a kinetic energy of 1467 eV, $1\sigma = 2.189$ nm, $3\sigma = 6.57$ nm

The addition of a heavier element, such as gold, on the surface shortens the IMFP, while the incorporation of a lighter element, such as oxygen, will lengthen the stated

IMFP. Using this information, we will later assess the thickness dependence of the oxide composition.

Table 3.1. Binding energies of different peaks of elemental gallium, GaAs, Ga_2O_3 and elemental arsenic as obtained experimentally in this study. Data from the NIST database (http://srdata.nist.gov/xps) is shown for comparison. In keeping with convention, only one of the peaks in the Ga 3p, Ga 3d and As 3d doublets is reported.

	Binding Energy [eV]							
	Ga (Expt.)	Ga (NIST)	GaAs (Expt.)	GaAs (NIST)	Ga_2O_3 (Expt.)	Ga_2O_3 (NIST)	As (Expt.)	As (NIST)
Ga $3d_{5/2}$	18.4	18.6 (± 0.3[4])	18.92	19.2 (± 0.4)	20.56	20.4 (± 0.5)		
Ga $3p_{3/2}$	103.9	104.5 (± 1.2)	104.37	104.8 (± 0.4)	105.64	105.6 (± 0.1)		
Ga $2p_{3/2}$	1116.5	1117.3 (± 0.8)	1117.02	1116.9 (± 0.1)	1117.70	1117.4 (± 0.5)		
As $3d_{5/2}$			40.89	40.7 (± 0.6)			41.55	41.4[5]
As $2p_{3/2}$			1322.63	1322.9 (± 0.2)			1323.29	1323.5 (± 0.4)

3.2.2 Composition of UV-Ozone Oxide

As shown in Figures 3.6 and 3.7, UV-ozone oxide mainly consists of Ga_2O, Ga_2O_3, As_2O_3, As_2O_5 and elemental As. Atomic quantification shows that the UV-ozone oxide of GaAs contains 22.2 atomic% of As of which 30.8% comes from metallic As, 67.1% from As_2O_3 and 2.1% from As_2O_5; and 23.6 atomic% gallium of which 50.4% corresponds to -As_xGa_2O, 43.8% to Ga_2O_3 and 5.7% to $Ga(OH)_3$. As_2O_3 is therefore the dominant component of the UV-ozone oxide layer.

---

[4] Standard deviation is calculated depending on the number of references available
[5] Only one reference is available
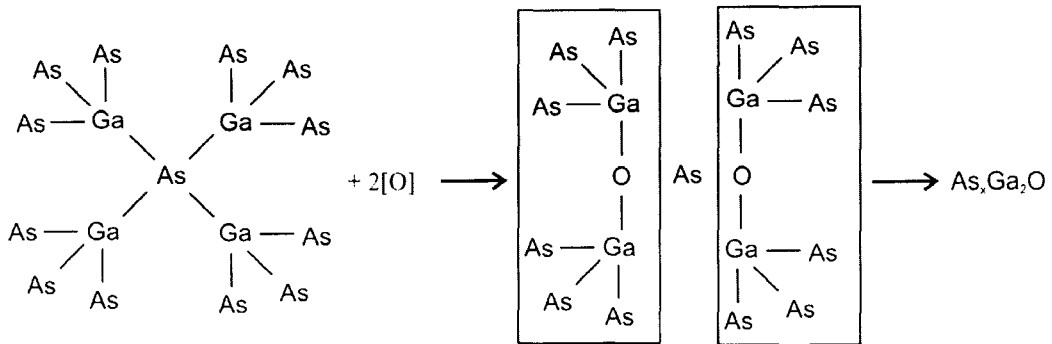
Figure 3.5. Formation of an intermediate species $-As_xGa_2O$ during the UV-ozone oxidation process in which Ga bonds with O by breaking one of its four bonds with As in GaAs, while retaining the remaining bonds. This process continues until eventually complete oxides are formed.

Atomic quantification appears to imply that the UV-ozone oxide is slightly Ga rich, contradicting the claims of an earlier report [77] that UV-ozone oxides of GaAs are As rich. A number of factors need to be considered here. Firstly, an inhomogeneous (gradual or layered) oxide film may appear richer in the component concentrated at the surface, because the signal from species buried below will be attenuated, depending on its IMFP. Secondly, the reliability of the deconvolution process of the spectra and its impact on the compositional numbers has to be examined. We initially deconvoluted our spectra excluding the contribution from $-As_xGa_2O$ which resulted in a relatively poor fit and the conclusion that UV ozone oxide has a 57% contribution from oxides of arsenic and elemental arsenic, and 43% from oxides of gallium. This would have implied an As rich UV-ozone oxide. Introducing an additional peak of $-As_xGa_2O$ at 19.7 eV resulted in a better fit and reduced the contribution of Ga (from GaAs) located at 19.37 eV thereby increasing the contributions from oxides of Ga. As a result, the UV-ozone oxide now appears slightly rich in Ga oxide. We conclude that within the limits of experimental

error (deconvolution process, signal attenuation) the oxide layer contains roughly equal

amounts of As and Ga.
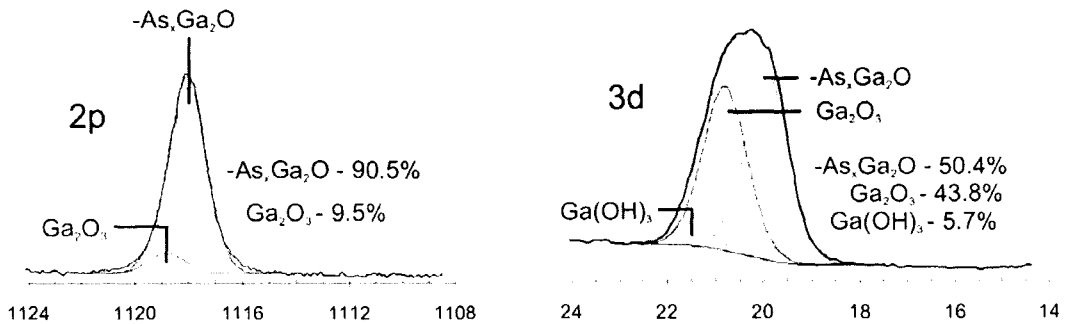
Figure 3.6. XPS spectra (Ga peaks) of UV-ozone oxidized GaAs, showing the presence of $-As_xGa_2O$, Ga_2O_3 and $Ga(OH)_3$ in the oxide layer. The contributions from different species as a percentage of total gallium are shown.

The 2p spectra are dominated by photoelectrons from the outermost layer of the

surface, because the high binding energy of the 2p electron results in a low kinetic energy

and hence a short IMFP. Thus, the information given by this region roughly refers to the

top few atomic layers, whereas As 3d spectra represent more of an average of the entire

oxide layer of the sample (taking into account attenuation of the signal from the lower

layers). The ratio of elemental As/As-oxide as obtained from 3d spectra is 1:2.2 whereas

it decreases to 1:8.4 for 2p spectra. This indicates that elemental arsenic is present mostly

at the interface with GaAs, which might be formed, as shown in Figure 3.5, due to the

breaking of arsenic bonds with gallium in the GaAs crystal lattice during the formation of

intermediate oxides of gallium. It has also been attributed to a photocarrier bond breaking

mechanism [77, 78] in which the Ga-As bond is speculated to be broken by promotion of

electrons from the valence band bonding orbitals to conduction band anti-bonding

orbitals, facilitating the diffusion and accumulation of As atoms near the interface.

Moreover, it can form due to a solid state interfacial reaction during the UV-ozone

oxidation process.
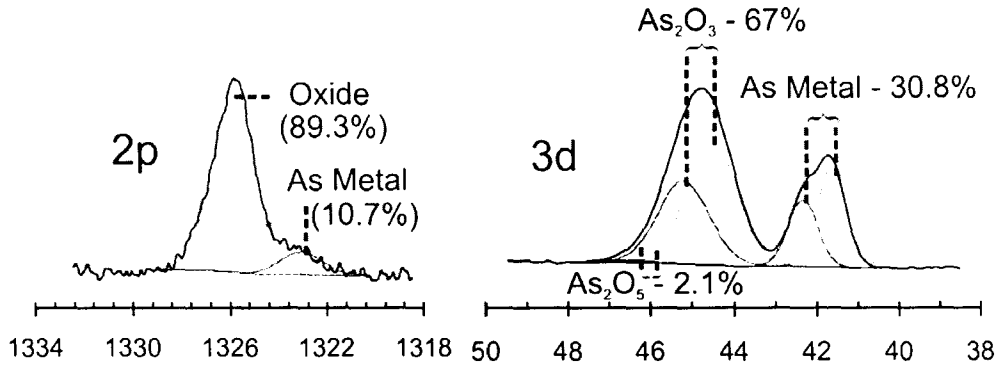
Figure 3.7. Arsenic high resolution XPS spectra from UV-ozone oxidized GaAs showing the contribution from different As components in the oxide layer. Relative contribution from different species as a percentage of total As is also shown.

The increased presence of oxide in the As 2p spectra (Figure 3.7) is an indication

of the presence of As_2O_5 on the surface of the oxide layer, which is generally attributed to

the extreme oxidation conditions [78]. Since growth of As_2O_3 is postulated to follow a

logarithmic behavior, the initially rapid growth rate of As_2O_3 into the sample slows down

gradually and As_2O_3 near the surface is starting to be converted to the higher oxide As_2O_5

under continuous exposure to oxidizing species.

In contrast, Ga 3d spectra show the ratio of Ga_2O_3 to $-As_xGa_2O$ to be

approximately 1:1.2, whereas for 2p spectra this ratio changes to 1:9.5. This decrease in

the ratio of Ga_2O_3 to $-As_xGa_2O$ suggests that Ga_2O_3 in UV-ozone oxide is formed deeper

inside the sample rather than in the surface region. Presence of gallium sub-oxide on the

surface of the UV-ozone oxide layer has been reported by various researchers [70, 79],

but unfortunately without a satisfactory explanation. If we assume that at the initial stage

of oxidation GaAs oxidizes directly to Ga_2O_3 (the most stable oxide of Ga) during UV-

ozone treatment, then the presence of Ga_2O on the surface could only be possible if

Ga_2O_3 is reduced to Ga_2O during the UV-ozone oxidation process.
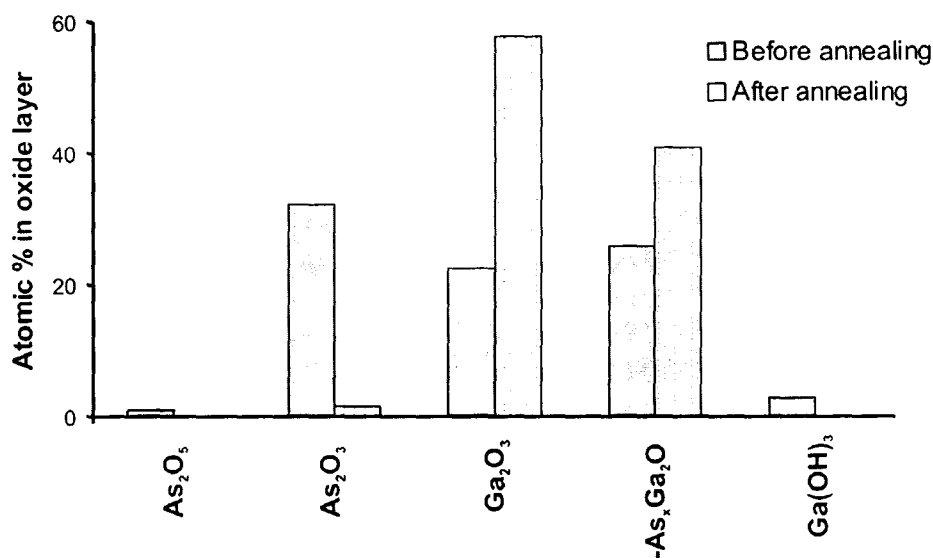
Figure 3.8. Effect of annealing on UV-ozone oxidized GaAs. Annealing at 500 °C for 300s results in complete desorption of $Ga(OH)_3$ and As_2O_5, eventually making the oxide layer rich in Ga_2O_3.

To explore this possibility, a standard Ga_2O_3 sample was treated with UV-ozone

for 20 minutes under the same conditions as employed for GaAs surface preparation.

High resolution XPS spectra from this sample did not show any measurable presence of

sub-oxide, leading us to conclude that Ga_2O_3 is not directly and by itself reduced to Ga_2O

by atomic oxygen species during UV-ozone oxidation. Consequently, as opposed to -

As_xGa_2O, As_2O_3 and As_2O_5, Ga_2O_3 may not be a product of UV-ozonation at all. Instead, Ga_2O_3 may form due to either of the following solid state chemical reactions:

$$3 -As_xGa_2O + 2 As_2O_3 \rightarrow 3 Ga_2O_3 + 4 As + 3 -As_x \qquad \text{Eq. 3.1}$$

$$As_2O_3 + 2 GaAs \rightarrow Ga_2O_3 + 4 As \qquad \text{Eq. 3.2}$$
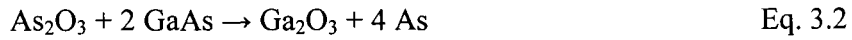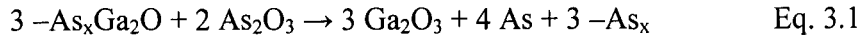
Given the heats of formation of Ga_2O_3 (-998.78 kJ/mol), As_2O_3 (-576.41 kJ/mol), As_2O_5 (-782.78 kJ/mol) and Ga_2O (-355.81 kJ/mol) [80], both reactions are thermodynamically favorable. The presence of elemental arsenic in the interfacial region, as mentioned above, also corroborates this mechanism. Thermodynamic equilibrium is not necessarily expected to be achieved during the UV-ozone oxidation process, since kinetics will drive this reaction. As we have found, UV-ozone oxide has a relative composition of 32.5 atomic% As_2O_3, 26.0 atomic% $-As_xGa_2O$ with 15.0 atomic% elemental As present mostly at the oxide-bulk interface. Even though the depletion of $-As_xGa_2O$ in the interfacial region would point to a substantial contribution of reaction (3.1) to the formation of Ga_2O_3, the localization of the process in the interfacial region would postulate an involvement of GaAs. Our data is insufficient to support further speculations about the mechanism of this process.

3.2.3 Effect of Annealing on UV-Ozone Oxide

Annealing of UV-ozone oxide has the overall effect of decreasing the amount of As in the oxide layer, thus increasing the proportion of Ga. Figure 3.8 shows the percentile composition of UV-Ozone oxide layer before and after annealing. Annealing UV-ozone oxide at 500 °C for 300 s results in complete desorption of $Ga(OH)_3$ and

As_2O_5, and partial loss of As_2O_3 due to desorption or reaction with other species, thereby making the film rich in Ga_2O_3. Presence of some As_2O_3 even after annealing at 500 °C is explained by trapping within the film, no matter whether its desorption temperature is assumed to be below 380 °C [81] or in the 400-500 °C range [82].

The sublimation point of the intermediate species $-As_xGa_2O$ is difficult to pinpoint. Since desorption of As from GaAs starts at 300 °C, it can be assumed that arsenic will be released from this intermediate species leading to the formation of Ga_2O which starts to desorb at 475 °C [83] or sublimes at temperatures above 500 °C [80]. Therefore partial desorption of Ga_2O due to annealing of UV-ozone oxide at 500 °C is possible. Since Ga_2O_3 has a very high sublimation point, desorption of Ga_2O_3 may only take place after reaction with bulk GaAs [71, 84]:

$$Ga_2O_3 + 4\,GaAs \rightarrow 3\,Ga_2O + 2As_2 \qquad\qquad Eq.\ 3.3$$
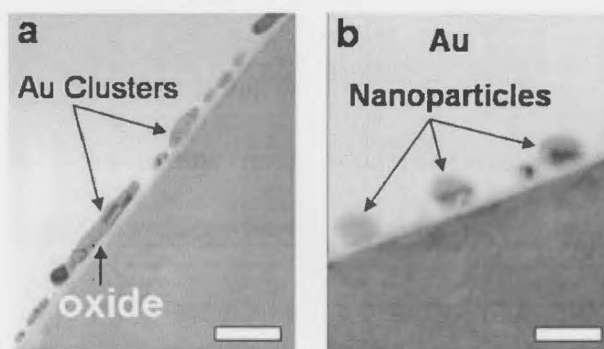
Figure 3.9. Cross-sectional view in TEM of UV-ozone oxidized GaAs after deposition of a nominally 4 nm thick gold film (a) before annealing and (b) after annealing. The scale bar corresponds to 20 nm.

Since desorption of Ga_2O starts at 475 °C and our samples were annealed at 500 °C, there could be partial decomposition, hence causing desorption of Ga_2O_3 from the

UV-ozone oxide layer. This is consistent with our 3d spectra, where the ratio of Ga_2O_3 to Ga_2O increases approximately from 1:1.15 to 1:0.7 due to annealing.

3.2.4 Formation of Au Nanoparticles

Figure 3.9 demonstrates that the gold film deposited on UV-ozone oxidized GaAs does not wet the surface. Instead, gold nanoparticles formed during annealing, with the reduction of surface energy acting as the driving force. Since the samples were annealed at 500 °C for 300 s, the diffusion of some gallium into the gold particles appears possible, which would result in an alloy.

The electronic structure of a metal particle critically depends on its size. For small particles, the electronic states are not continuous but discrete due to confinement of the electron wavefunction which consequently changes the binding energy of the core electrons. This change in binding energy depends on the type of material. For gold clusters, it does not change significantly (~0.1 eV) until a critical size of about 3 nm [85]. Since the average particle size in our study is about 4.5±1.4 nm, no change in binding energy will be expected due to the size effect. The binding energy of the gold in the nanoparticles also changes as a result of alloying, for example with gallium. Literature data (Table 3.2) indicates that a chemical shift in the Au $4f_{7/2}$ peak of 0.56 eV occurs even in the case of only 12 atomic% of Ga in the Ga-Au alloy. The Au 4f binding energy increases with increasing concentration of gallium in the alloy. Figure 3.10 shows XPS spectra obtained from gold nanoparticles formed on different oxide thicknesses, with the data corrected to carbon 1s at 284.80 eV.
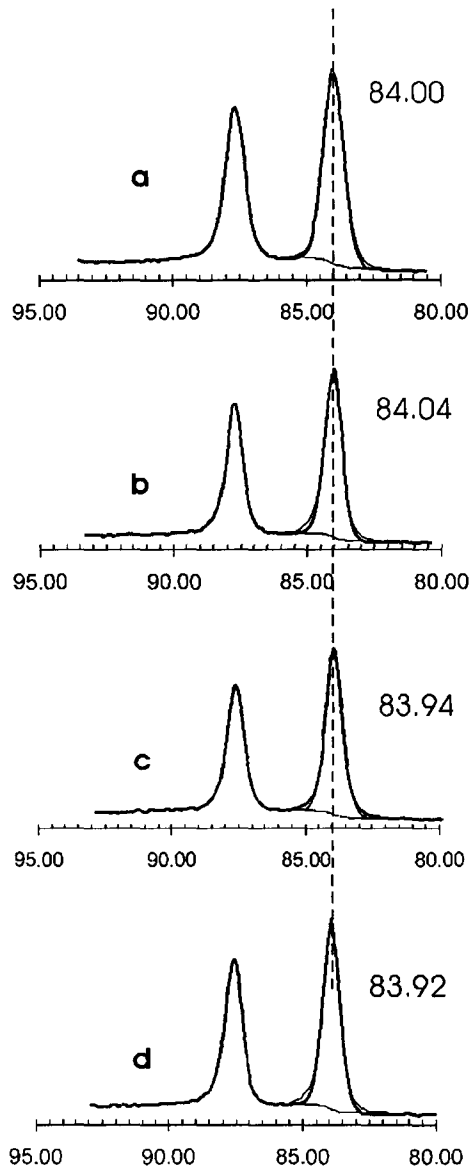
Figure 3.10. Au $4f_{7/2}$ peaks obtained from samples (a) before and (b) after the formation of Au nanoparticles on UV-ozone oxides having a thickness of 3.5 nm. Samples with oxide thicknesses of (c) 2.5 nm and (d) 4.5 nm are also examined after annealing. As indicated by the dotted line, there is no significant chemical shift in the Au peak, indicating Au does not make an alloy with Ga.

47

Table 3.2. Literature values for the binding energy of Au $4f_{7/2}$ for different compositions of AuGa. (from the NIST database http://srdata.nist.gov/xps)

Line	Au metal	$Au_{88}Ga_{12}$	$Au_{78}Ga_{22}$	Au_9Ga_4	$Au_{50}Ga_{50}$	$AuGa_2$
Au $4f_{7/2}$	83.96 eV	84.4 eV	84.64 eV	84.91 eV	85.29 eV	85.56 eV

The binding energy is found to be 84.00 eV, 84.04 eV, 83.94 eV and 83.92 eV in the cases of unannealed gold on 3.5 nm oxide, annealed gold on 3.5 nm, 2.5nm and 4.5 nm oxide, respectively. All these values are characteristic of bulk elemental gold, as becomes clear by comparison to Table 3.2. Even for a decreased oxide thickness of 2.5 nm, XPS spectra do not show any chemical shift, giving very strong indication that gold does not alloy with gallium during the formation of Au nanoparticles, within the detection limit of XPS (~1-2%).

In order to confirm the lack of alloying of gold with gallium, electron energy loss spectroscopy (EELS) was carried out using HRTEM. Since deposition of a gold film of 1 nm leads to the formation of particles of around 4 nm diameter, it is near impossible to perform EELS using HRTEM due to instrumental drift during spectra acquisition. For accurate and reliable data, a gold layer of 4 nm was deposited onto the oxide layer that resulted in the formation of larger Au nanoparticles [41] after annealing. Figure 3.9 shows the cross-sectional TEM view in which the Au layer is clearly separated from the substrate by a thin layer of UV-ozone oxide. The gap between the Au clusters is a manifestation of the de-wetting process of Au on the oxide layer, resulting in nanoparticles having a size of around 15 nm after annealing. A study of compositional

analysis with EELS-HRTEM gave no indication of the presence of any gallium in the gold particles, even at this larger particle size [41].

Previously, the presence of approximately 20 atomic% Ga in much larger gold particles was reported as measured by energy dispersive X-ray (EDX) analysis [41]. These results can be conciliated with each other by considering the difference in sample preparation between the two studies. Apart from possible size effects, it is also important to consider that the sample subjected to EDX analysis in the previous case was etched with HF to remove the UV-ozone oxide before Au deposition. Since the layer of Au was only separated from the substrate by a thin native oxide layer, the formation of an alloy between gold and gallium during annealing may be more facile. In the case of our current study, however, gold was sitting on top of the oxide layer and alloying would only be possible if gallium from the bulk was to diffuse through the oxide layer to the gold particles. Since both XPS and EELS confirm that gold does not form an alloy with gallium, it can be assumed that out-diffusion [81] of gallium into gold through the oxide layer is not possible under the present annealing conditions.

3.3 Chapter Summary

We have studied the annealing process of UV-ozone oxide on GaAs for the purpose of gold nanoparticle formation. UV-ozone oxide consists of Ga_2O_3, $-As_xGa_2O$, $Ga(OH)_3$, As_2O_3, As_2O_5 and elemental As. In our understanding, the oxide layer is neither a strictly layered structure with sharp interfaces nor does it consist of a single phase of oxides having different compositions. The UV-ozone oxide layer has a complex

physical structure with Ga_2O_3 and elemental As residing close to the substrate while the concentration of $-As_xGa_2O$ increases at the surface with a layer of As_2O_5 on top, and As_2O_3 distributed all through the oxide layer.

Annealing UV-ozone oxide at 500 °C for 300 s results in complete desorption of As_2O_5 and $Ga(OH)_3$ and partial desorption of As_2O_3 and Ga_2O making the oxide layer rich in Ga_2O_3. We postulate the presence of an intermediate oxide $-As_xGa_2O$ based on the atomic arrangement in the GaAs crystal lattice. The evolution of As, Ga_2O_3 and also Ga_2O has been explained based on this assumption. It has also been proposed that Ga_2O_3 is not a direct species of the UV-ozonation process; rather it is produced due to reaction between oxides arising from the UV-ozone process or reaction of As_2O_3 with the bulk substrate.

Analysis using XPS shows that gallium does not form an alloy with gold in nanoparticles as confirmed by EELS-HRTEM measurement. If there is any amount of gallium present in the gold particles, it was below the detection limits (1-2%) of XPS and EELS.

Chapter 4

Role of Proximity Caps during Annealing

This section provides a deeper insight into the chemistry and physics of the common engineering practice of using a proximity cap while annealing compound semiconductors such as GaAs. It explores the role played by the capping material during the annealing of UV-ozone oxide and also during the formation of gold nanoparticles. During the annealing of UV-ozone oxidized GaAs, it has been observed that GaAs proximity caps also serve as a sacrificial layer to accelerate the desorption of oxide species. Deposition of a thin layer of gold and subsequent annealing to 500 °C for 300 s under different capping conditions show the use of a proximity cap to be practically insignificant in annealing Au deposited films. However, in both cases surface deterioration due to pit formation has been observed and the depth of pits is found to depend on the effective role played by the capping material. Moreover, capping material dependence of pit formation of GaAs surface has also been discussed.

4.1 Introduction

In thermal processing of GaAs and other compound semiconductors, it is important to inhibit the loss of volatile components such as arsenic, resulting in changes in the stoichiometry, conductivity and mobility of charge carriers in the bulk material. The use of an encapsulating layer of a dielectric film, such as SiO_2 or Si_3N_4, can effectively inhibit the loss of As from the bulk and help maintain the integrity of the semiconductor-oxide interface up to high temperatures [86]. The tight enclosure of the sample becomes a problem, however, in cases where the annealing procedure serves to form nanoparticles [41, 42]. Alternatively, an arsenic overpressure in the annealing vessel can be provided as a background from an arsenic cell, or a local overpressure can be created by covering the wafer in close contact with another Si [87] or GaAs [88] wafer. This method of using an additional wafer face-to-face, generally known as a proximity cap, relies on trapping the arsenic that was lost during annealing at the interface between the cap and the GaAs wafer. The entirety of this chapter is published in the Journal of Applied Physics [43], and it discusses the role of proximity caps during the formation of gold nanoparticles which will be used for the growth of nanowires in the VLS mechanism.

4.2 Experimental Details

Epi-ready n-type GaAs (100) wafers (Wafer Technology Ltd.) having a carrier concentration of $(1-5) \times 10^{18}$ cm^{-3} were used as the substrate material. These were oxidized in a UVOCS UV/ozone reactor in order to remove hydrocarbon contamination and to

produce an oxide layer whose thickness was determined by the oxidation time. After UV-ozone oxidation for 20 minutes (corresponding to 3.5 nm thick oxide), the sample was transferred to an electron beam evaporation system. A gold film with a nominal thickness of 1 nm was deposited on UV-ozone oxidized samples at room temperature using the e-beam evaporation system at a pressure of 10^{-8} Torr at an average rate of 0.1 nm/s, as monitored by a quartz crystal monitor. Annealing was carried out at 500 °C for 300 s in a N_2 environment using an AG Associates Mini-Pulse rapid thermal annealing (RTA) furnace at a typical ramp rate of 1 °C/s. Both GaAs and Si proximity caps were used during annealing of the samples, and annealing was also carried out without any capping material. All caps used during annealing were also subjected to XPS. A brief sample description together with atomic quantification based on XPS survey spectra of the core lines Ga 3d, As 3d, Au 4f and O 1s of all these samples are summarized in Table 4.1. Series A contains all the samples having only UV-Ozone oxide before and after annealing at 500 °C for 300 s under different capping conditions. Series B contains samples with a 1 nm Au layer on top of the UV-ozone oxide before and after annealing under different capping conditions. A peak due to adventitious carbon was detected, but excluded from the analysis.

Cross-sectional imaging of the samples was done on a Philips CM12 transmission electron microscope. A JEOL JEM-2010F TEM was also employed for chemical analysis via energy dispersive X-ray spectroscopy (EDXS).

4.3 Results and Discussion

In order to correctly assign the peaks in the case of small chemical shifts for different states of an element (in particular Ga) and to establish a baseline of our work, a standard GaAs substrate, Ga_2O_3 and As metal were subjected to XPS measurement [42]. Binding energies, as obtained, associated with different peaks are: for GaAs, Ga $3d_{5/2}$ at 18.92eV, Ga $3p_{3/2}$ at 104.37 eV, Ga $2p_{3/2}$ at 1117.02 eV; for Ga_2O_3, Ga $3d_{5/2}$ at 20.07 eV, Ga $3p_{3/2}$ at 105.61 eV, Ga $2p_{3/2}$ at 1117.4 eV and for As, As $3d_{5/2}$ at 41.55 eV.

A survey of the available literature [67] shows that binding energies associated with different peaks are within the previously reported range of energies. All spectra were charge corrected to the main line of carbon 1s (C-C and C-H from adventitious carbon) set to 284.8 eV.

Table 4.1 shows that UV-ozone oxidized GaAs consists of 23.6 atomic% Ga and 22.2 atomic% of As with the balance made up of oxygen. Depositing a layer of Au on UV-Ozone oxide causes attenuation of the XPS signal from the oxide film, but the ratio of Ga to As remains approximately constant. Regardless of the capping material, all the samples exhibit an increase in the relative amount of Ga and a pronounced decrease in the amount of As together with slight reduction in the amount of O. An attenuation of the gold signal in the B series samples is observed due to the change in the morphology of the gold, even though the total amount of gold likely stayed constant. Because the gold nanoparticles formed after annealing are on average 4.5nm in diameter as opposed to the original thickness of 1 nm, the average gold signal has to penetrate a thicker layer of gold than the signal from the film before annealing, thereby causing attenuation.

Table 4.1. Atomic quantification based on survey spectra from different samples. Series A comprises the samples having only UV-Ozone oxide and Series B comprises all the samples with a Au layer. All UV-Ozone oxides have a thickness of 3.5 nm. Annealing took place at 500 °C for 300 s. A 1 nm thick Au film was e-beam evaporated on all samples in Series B. Percentages given are atomic%.

	As 3d	**Ga 3d**	**O 1s**	**Au 4f**
Series A:				
GaAs (100) + Oxide	22.2%	23.6%	54.3%	n/a
... annealed with GaAs cap	12.5%	37.4%	50.1%	n/a
... annealed with Si cap	13.5%	37.0%	49.6%	n/a
... annealed without cap	16.4%	37.9%	45.7%	n/a
Series B:				
GaAs (100) + Oxide + Au	11.9%	13.8%	53.0%	21.3%
... annealed with GaAs cap	7.2%	32.0%	42.3%	18.5%
... annealed with Si cap	7.0%	32.0%	42.6%	18.4%
... annealed without cap	7.0%	33.5%	43.3%	16.3%

4.3.1 Effect of Capping on Bare Oxide

The UV-ozone oxide of GaAs consists of 22.2 at. % of As of which 30.8% comes from metallic As, 67% from As_2O_3 and 2.1% from As_2O_5, and 23.6 atomic% gallium of which 50.4% corresponds to suboxides, 43.8% to Ga_2O_3 and 5.7% to $Ga(OH)_3$. Gallium suboxides may include any species of the type $-As_xGa_2O$ in which two gallium atoms
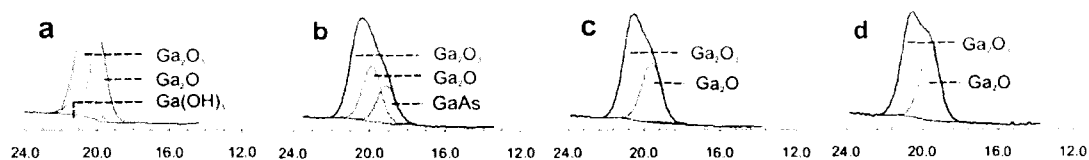
Figure 4.1. High resolution Ga 3d spectra show the effect of annealing on UV-Ozone oxidized samples at 500°C for 300s - (a) annealed with a GaAs cap, (b) annealed with a Si cap, and (c) annealed without a cap. The presence of a peak originating from bulk GaAs in case of the sample annealed with a GaAs proximate cap is indicative of a decrease in the oxide layer thickness.

that are bridged by one oxygen atom are also back-bonded to arsenic atoms that were part of the original GaAs network, or mixed oxide species in which an oxygen atom was inserted into a Ga–As bond of the original GaAs structure [42]. Regardless of the type of proximity cap used, it was found that As_2O_5 and $Ga(OH)_3$ are removed from the oxide layer after annealing the sample at 500 °C for 300 s. High resolution spectra (Figure 4.1) show that the relative contribution of Ga_2O_3 to the gallium signal has significantly increased as compared to the unannealed sample (Figure 4.1(a)), regardless of capping material. While the Ga 3d spectra in the case of the Si cap (Figure 4.1(c)) and without cap (Figure 4.1(d)) resemble each other, a contribution from the bulk GaAs emerges in the case of the GaAs cap (Figure 4.1(b)). This is indicative of a significant thinning of the oxide layer. In the high-resolution As 3d spectra, a corresponding effect is observed (Figure 4.2) in comparison with the unannealed sample (Figure 4.2(a)). While the arsenic oxide contribution is strongly reduced in all three cases, the majority of the arsenic signal results from either bulk GaAs in the case of a GaAs capped sample (Figure 4.2(b)) or elemental arsenic in the case of the Si capped or uncapped samples (Figures. 4.2(c) and

56

4.2(d) respectively). A peak originating from As 3d photoelectrons from GaAs must be accompanied by a corresponding peak of comparable intensity from Ga 3d photoelectrons due to their similar kinetic energy and therefore similar inelastic mean free path. Comparison of the Ga 3d and As 3d peak intensities show that approximately 2/3 of the lower energy As 3d signal should correspond to GaAs, whereas 1/3 is left to be attributed to metallic arsenic. Indeed, deconvolution of As spectra obtained from annealed UV-Ozone oxide including the contribution of elemental As shows that 19.8% of total As comes from elemental As, whereas 78.5% originates from bulk GaAs together with 1.7% from As_2O_3.
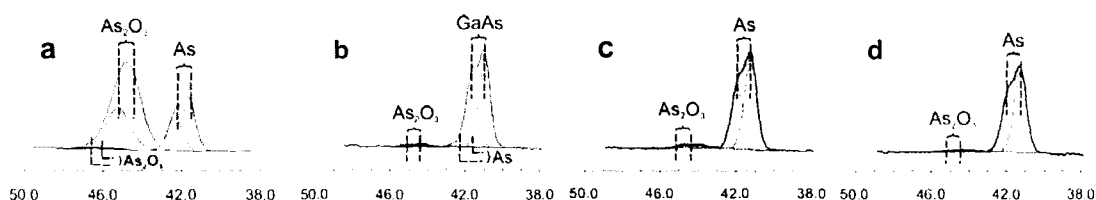
Figure 4.2. High resolution As 3d spectra from UV-Ozone oxidized samples that have been annealed at 500 °C for 300s - (a) unannealed sample for comparison, (b) annealed with a GaAs cap, (c) annealed with a Si cap, and (d) annealed without a cap. A strong peak from elemental As in the cases of annealing with a Si cap and without a cap points to a significant reaction taking place at the bulk - oxide interface.

When UV-ozone oxidized GaAs (100) is annealed with a GaAs cap, the oxide layer may react with GaAs both from the bulk and from the cap according to the following solid state chemical reactions:

$$As_2O_3 + 2\ GaAs \rightarrow Ga_2O_3 + 2\ As_2\uparrow \qquad\qquad Eq.\ 4.1$$

$$As_2O_3 + 6\ GaAs \rightarrow 3\ Ga_2O + 4\ As_2\uparrow \qquad\qquad Eq.\ 4.2$$

57
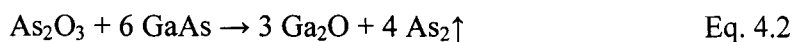
"Ga$_2$O" in reaction (4.2) may also stand for any suboxide species as described previously. GaAs, $-As_xGa_2O$ and Ga$_2$O$_3$ all contain gallium in the formal oxidation state of +3, even though the Ga–As bond in GaAs has a very strong covalent character as opposed to the ionic bonding arrangement in Ga$_2$O$_3$. $-As_xGa_2O$ can be seen as an intermittent arrangement. Ga$_2$O in contrast contains gallium in the less favorable formal +1 oxidation state, but may become relevant in oxygen poor conditions when no arsenic atoms are available to satisfy additional valences.

The evolution of arsenic vapor as As$_2$ or As$_4$ depends on the circumstances and has no bearing on the fate of the oxide film. Since the formation of arsenic vapor starts at 300 °C [83, 89], an overpressure is created in the case of the GaAs cap that inhibits the loss of As from the substrate material. Arsenic at the interface between the oxide film and the underlying bulk GaAs is trapped below the oxide film and therefore unable to escape, as supported by the data in Figures 4.2(c) and 4.2(d). In addition to creating an overpressure, arsenic oxides of the film also react with GaAs from the nearby cap, contributing to a reduction of the thickness of the oxide layer. The composition of the oxide films before and after annealing under different capping is summarized in Figure 4.3 in which relative atomic percent of different species has been calculated by analyzing the percentile contribution of each species (obtained from high resolution spectra) to the overall presence of the corresponding element as determined from survey spectra (Table 4.1). The Ga$_2$O$_3$ formed at the interface of the oxide layer and a GaAs cap will reside at the cap, whereas Ga$_2$O$_3$ formed at the interface of the oxide layer and the underlying bulk GaAs will be part of the sample. Therefore, the data summarized in Figure 4.3 shows a

lower amount of Ga_2O_3 in the case of GaAs cap annealing, in contrast to the cases of Si-capped and uncapped samples.
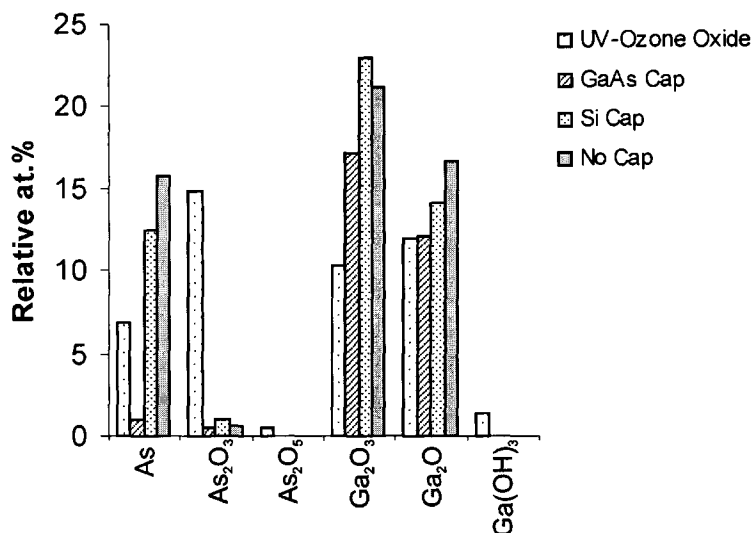
Figure 4.3. Change in relative atomic concentration of different species of UV-Ozone oxide layer before and after annealing at 500 °C for 300 s under different capping conditions, which shows that regardless of capping conditions, As_2O_5 and $Ga(OH)_3$ completely disappear after annealing. Relative atomic percent of different species has been calculated by analyzing the percentile contribution of each species to the overall at. % presence of corresponding elements, as calculated from survey spectra (Table 1).

In the cases of Si capping and 'no- capping', there are no significant contributions from bulk GaAs in either the Ga or the As spectra. In both cases, there are no reactants from the cap available to assist in decomposition and desorption of the oxide. Instead, the oxide film reacts with the bulk GaAs substrate, resulting in pit formation. It appears that GaAs capping material not only serves to reduce the loss of As but also acts as a sacrificial layer for oxide desorption.

It has been suggested [90, 91] that at or above 500 °C there is a possibility of Ga_2O_3 from the oxide layer reacting with Ga from bulk GaAs to produce gallium suboxide and elemental arsenic:

$$Ga_2O_3 + 4\,GaAs \rightarrow 3\,Ga_2O + 2\,As_2\uparrow \qquad\qquad Eq.\ 4.3$$
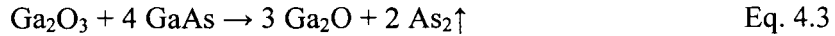
This in turn would cause depletion of Ga from the bulk and the remaining As could be removed in the form of As_2 and As_4 from the bulk material. Since Ga_2O has a desorption temperature of more than 500 °C, increased presence of Ga_2O in the oxide after annealing may be to attributed to this chemical reaction. Another likely source of Ga_2O is reaction (4.2) above.

All three reactions outlined above increase the amount of elemental As, which is drastically observed in the case of annealing with Si cap and without capping. This shows that those reactions occurred at the oxide-bulk interface, where As is blocked from evaporating by the oxide overlayer. In the case of the GaAs cap, the amount of remaining elemental arsenic is significantly less than in the other two cases. From our analysis of the various arsenic peaks it becomes clear that annealing has the effect of reducing the amount of arsenic oxide in the oxide layer, therefore increasing the relative amount of gallium oxide.

4.3.2 Effect of Annealing on Au Covered Oxide

Annealing of a 1 nm thick Au layer deposited on UV-Ozone oxide results in the formation of Au nanoparticles of an average size of 4.5±1.4 nm [41]. As shown in Table 4.1, annealing has the overall effect of decreasing the total As and increasing Ga in the

oxide layer irrespective of the capping material used. The reasons for this have been discussed in the previous section.
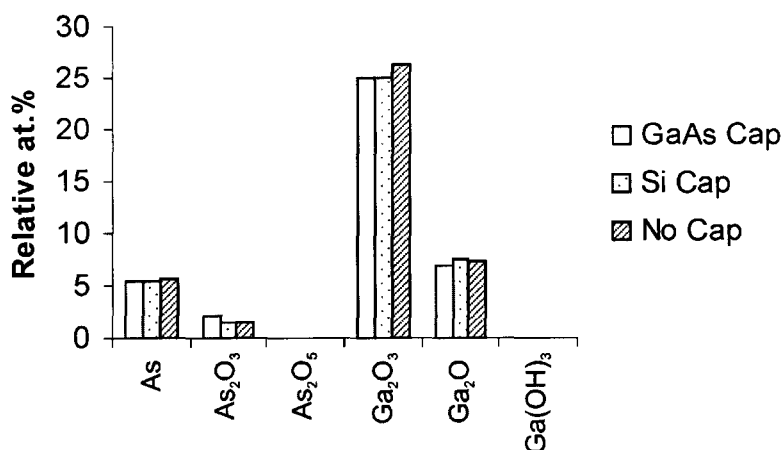
Figure 4.4. Relative atomic concentration of different species after annealing of Au coated UV-Ozone oxide at 500 °C for 300 s in which relative atomic percent of different species has been calculated by analyzing the percentile contribution of each species to the overall at.% presence of corresponding elements, as calculated from survey spectra (Table 4.1). Irrespective of capping conditions, As_2O_5 and $Ga(OH)_3$ were completely desorbed from the sample.

The decrease in the Au signal, as mentioned earlier, is due to formation of Au nanoparticles, hence changing the average attenuation of the Au signal while the total amount of Au atoms stays constant. A slight decrease in the oxygen content may be due to the desorption of oxides from the UV-ozone oxide layer.

However, high resolution XPS spectra reveal that the relative amount of different species (Figure 4.4) present after annealing remains almost the same regardless of capping mechanism and it seems that capping has no effect in annealing GaAs when it is covered by a layer of an inert material such as gold. This can be understood by

considering the gold layer as a cap layer during the annealing process, which in effect not only prevents the proximity cap from reacting with the different oxides but also works as a partial barrier layer against desorption, much like the encapsulating layers described earlier [86]. However, its efficiency will be much less than a traditional encapsulating layer due to the nanoparticle formation, which exposes significant parts of the surface. A slight increase in the observed amount of As_2O_3 compared to series A may be due to the trapped species that were unable to desorb from underneath the Au layer.
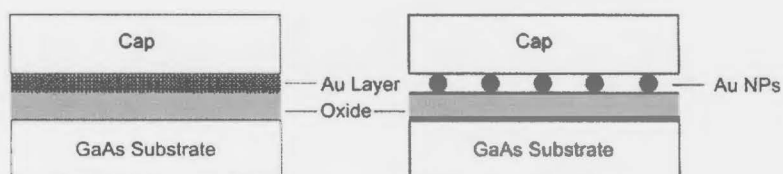
Figure 4.5. Schematic showing how the proximate caps used in annealing Au deposited UV-Ozone oxide are separated from the oxide layer by a layer of Au that leads to the formation of Au nanoparticles during annealing.

All proximity caps used during this experiment were also studied by XPS, but only survey spectra were recorded. Atomic quantification from the GaAs caps shows a two-fold increase in the Ga to As ratio, corresponding to an increase of Ga content by 25% and decrease of As content by 34% with respect to standard GaAs samples. The loss of As mainly occurs due to the higher vapor pressure of As over Ga in GaAs. Si caps do not show any presence of Ga or As and remain practically inert during the annealing process.

However, annealing GaAs (100) under all conditions studied leads to the formation of surface pits because of the interfacial reactions between GaAs and other

reacting species present in the oxide layer. The presence of step-edges and kinks act as energetically favorable sites for reaction [84], which lead to faceting and, eventually, the formation of surface pits. In the case of annealing UV-ozone oxide with a GaAs cap, oxides make use of GaAs material both at the substrate (bottom) and cap (top) interfaces, with the substrate and the cap effectively serving as sacrificial layers for the desorption to take place. On the other hand, as illustrated in Figure 4.5, when the oxide layer is covered with a layer of Au, oxides cannot react with GaAs from the cap. Instead they react solely with the substrate material, leading to the formation of pits much deeper than those resulting from annealing bare UV-ozone oxide films.

It has been observed that pits formed due to the annealing of UV-ozone oxide with a GaAs cap are around 2-3 nm deep, whereas pit depth can increase up to 14 nm for series B (Figure 4.6). This also supports the idea of a reaction between the oxide layer and the GaAs bulk being responsible for the formation of volatile species that subsequently desorb.

In order to verify the chemical composition of the pits, a cross-sectional sample was line-scanned along the pit using EDXS with the beam diameter set to ≤1nm and with a line scan dwell time of 2 ms. Data was taken for a total of 500 frames with each frame taking 6.55 s to record. As shown in Figure 4.6, there is an increase in As peak intensity at the pit-GaAs bulk interface and there is no contribution from O at the interface area. This confirms the presence of elemental As at the interface. As we move into the oxide layer, the relative intensity of gallium increases and at the same time the O signal intensifies, indicative of the presence of gallium oxide in the pit. We conclude that the pit

mainly consists of elemental As and gallium oxide, having elemental As at the interface. The EDXS spectra also show that the UV-ozone oxide layer becomes Ga rich upon annealing, consistent with the XPS data presented in this study. However, an analysis of pit formation on GaAs (100) substrates, subjected to different surface preparations, will be covered in greater detail in the next chapter.
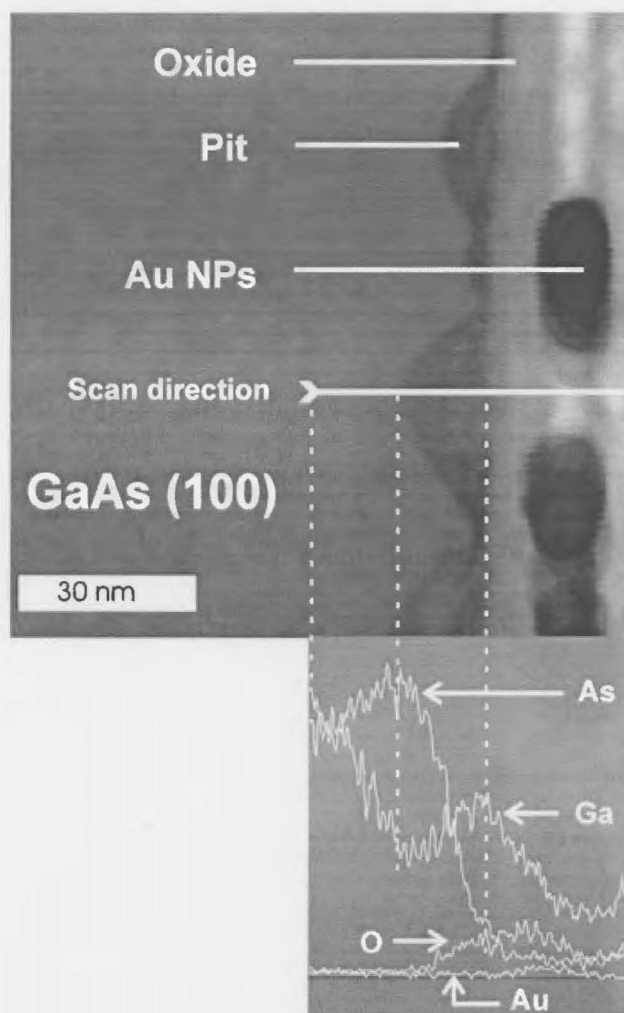
Figure 4.6. EDXS spectra obtained from a cross-sectional sample showing the formation of surface pits in the gold coated oxide layer during annealing. Pits have different depths and consist of elemental As and Ga_2O_3, with elemental As at the interface.

4.4 Chapter Summary

The role and efficiency of proximity caps during the annealing of UV-ozone oxide, and the evolution of monodisperse Au nanoparticles on UV-ozone treated GaAs (100) substrates, has been studied under different capping conditions using X-ray photoelectron spectroscopy. It has been shown that the effectiveness of proximity caps depends on the geometry and structure of the sample. GaAs proximity caps used in annealing UV-Ozone oxidized GaAs have the advantage of acting as a sacrificial layer in addition to creating a local overpressure of As that inhibits the loss of arsenic from the sample. In the case of gold coated UV-Ozone oxide, it has been found that the proximity caps play no significant role in annealing the sample at 500 °C. Deterioration of GaAs (100) surface occurred in both cases due to the formation of pits and the latter has pits much more deeper due to reaction of the oxide layer with the substrate material. EDXS shows that pits mainly consist of elemental As and Ga_2O_3 with elemental As at the pit oxide interface. However, presence of small amount of As_2O_3 cannot be ruled out.

Chapter 5

Effect of Surface Preparation on Nanowire Growth

This chapter discusses the influence of GaAs (100) substrate preparation on GaAs nanowire growth. By pre-treating the substrate under different conditions, surface topography and distribution of seed particles prior to nanowire growth as well as density and growth direction of nanowires have been analyzed. It will be shown that both density and orientation of nanowires are strongly influenced by the topography of the GaAs (100) substrate prior to growth. The change in topography occurs due to the formation of pits of various size and orientation as a result of interaction with gold and oxides. The onset of nucleation of nanowires has been related to the relative position of seed particles on the substrate. The content of this chapter has been published in Nanotechnology [44].

5.1 Experimental Details

Epi-ready n-type GaAs (100) substrates (supplied by Wafer Technology Ltd.) having a carrier concentration of $(1-5) \times 10^{18}$ cm^{-3} were subjected to various surface preparations prior to depositing Au for metal-assisted nanowire growth. In particular, UV-ozone oxidation is a common method for removal of hydrocarbons prior to epitaxial growth. Therefore, three surface treatments were investigated:

1) Treatment A consisted of the as-received Epi-ready wafer with no further processing.

2) Treatment B consisted of a 20 minute UV-ozone oxidation of an Epi-ready wafer using a UVOCS UV-Ozone reactor.

3) Treatment C consisted of the identical treatment as B but followed by a 30 second buffered HF etch.

In all cases, samples were loaded immediately into an e-beam evaporator following treatment, for room temperature deposition of 1 nm of Au as measured by a quartz crystal thickness monitor. After Au deposition, the wafers were loaded into a gas source MBE chamber where substrates were annealed at 500 °C for 5 minutes followed by surface cleaning and oxide desorption with an in-situ inductively coupled hydrogen plasma at 550 °C for 10 minutes. Thermal annealing and plasma cleaning occurred under an excess As$_2$ pressure supplied by cracking AsH$_3$ at 950 °C. Substrates were then either removed for characterization, or nanowire growth was carried out by opening the Ga effusion cell shutter. Growth occurred for up to 20 minutes at a typical 2-D growth rate of 1 µm h^{-1} with a V/III flux ratio of 1.5 at 500 °C.

A JEOL JSM-7000F field emission scanning electron microscope (SEM) was employed to measure the tilt angle of the nanowires relative to the substrate surface in cross-sectional views. The distribution of nanowire growth directions was determined by in-situ tilting of the samples in the SEM, as described in section 2.2.2.1, until a subset of nanowires with a particular growth direction was oriented along the viewing direction parallel to the electron beam, i.e., until only a gold particle at the top of the nanowires appear as bright spots. The nanowire growth direction relative to the substrate was then determined by the measured tilt angle and the number of nanowires growing in that particular direction was counted as spots visible in the SEM image. Thus the overall distribution of nanowire growth directions could be determined by measuring several hundred nanowires in this manner.

Compositional analysis of the samples was performed by energy-dispersive X-ray spectroscopy (EDXS) in a JEOL-JEM-2010F high resolution transmission electron microscope (HRTEM). TEM samples were prepared by manual polishing followed by Ar milling with a Gatan precision ion polishing system (Model 693).

5.2 Results

After thermal annealing and plasma cleaning, the variously treated surfaces were removed from the MBE chamber (without nanowire growth) for SEM and TEM analysis. Plan view SEM images in Figure 5.1(a), (b), and (c) for the A, B, and C treatments, respectively, revealed Au particles (bright areas) and pits (dark areas). The size and

orientation of the pits depended on the surface treatment. Cross-sectional TEM images in Figures 5.1(d)-(f) for the three surface treatments indicated that the sides of the pits parallel to the [011] direction consisted of (11-1) and (1-11) planes (B planes), while TEM images along the orthogonal direction (not shown) indicated that the sides of the pits along the [01-1] direction consisted of (111) and (1-1-1) planes (A planes), consistent with prior observations [92]. The Au particles were found to be dispersed on the surface both inside and outside of the pits. The orientation and lateral dimensions of the pits were measured directly from plan view SEM images, while the depth of the pits was
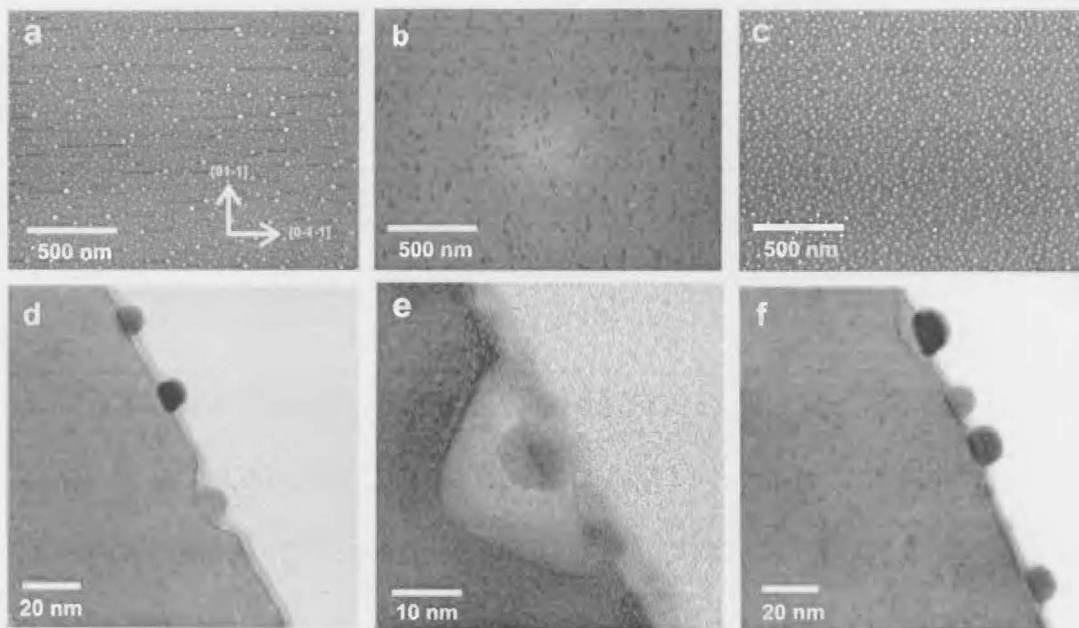
Figure 5.1. Plan view SEM images (top row) and HRTEM images viewed along the [011] direction (bottom row) after thermal annealing and plasma cleaning for ((a), (d)) treatment A (Epi-ready); ((b), (e)) treatment B (UV-ozone); and ((c), (f)) treatment C (UV-ozone/HF-etch).

assessed from cross-sectional TEM images for the three surface treatments. Treatment A resulted in the formation of pits elongated along the [011] direction having an average

length of 325 nm with depth in the range of 8 to 12 nm. Pits on the C-treated surface, having an average length of 65 nm, were also elongated along the [011] direction, but were shallower (4 to 6 nm range). On the other hand, pits on the B-treated substrate appeared to be elongated along the [01-1] direction, perpendicular to the previous two cases with an average length of 74 nm with varying depth ranging from 7 to 13 nm.

An analysis of the catalyst size distribution after thermal annealing and plasma cleaning of the A-, B- and C-treated surfaces was carried out, as shown in Figure 5.2, by direct measurements in SEM and TEM images (such as those in Figure 5.1). Au particles on Epi-ready (treatment A) and UV-ozone (treatment B) surfaces had a narrow size distribution, whereas particles on HF-etched surfaces (treatment C) spanned a long range of sizes having an average size much larger than those grown on Epi-ready and UV-ozone treated GaAs (100) substrates. The smallest particles, having an average diameter of 5.8 nm, were found to grow on the B-treated substrate at a density of $5.5 \times 10^{11}/cm^2$. On Epi-ready substrates, an average diameter of 8.3 nm was obtained, slightly higher than the B-treated substrate, corresponding to a decrease in density to $2.1 \times 10^{11}/cm^2$. Finally, particles grown on HF–treated substrates (treatment C) spanned the widest range of sizes with an average of 17.6 nm and the lowest density of $8.8 \times 10^{10}/cm^2$.

To further understand the formation process of the pits, TEM and EDXS analysis was performed on the UV-ozone treated sample (treatment B) after thermal annealing at 500 °C for 300 s. Cross-sectional HRTEM images, for example in Figure 5.3(a), indicated the presence of pits as observed previously in Figure 5.1.
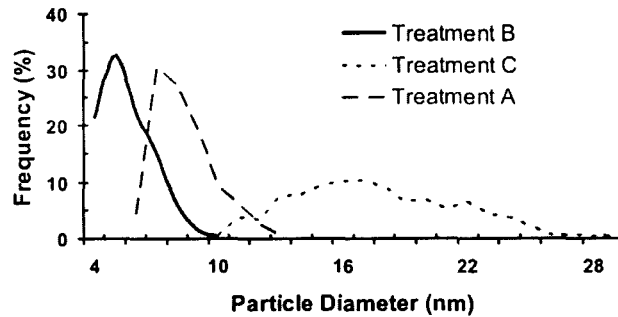
Figure 5.2. Au particle size distribution after treatment A (Epi-ready), treatment B (UV-ozone), and treatment C (UV-ozone/HF etch).

EDXS linescans were used to determine the chemical nature of the pits and the UV-ozone oxide. An EDXS linescan, shown in Figure 5.3(c), was performed across the pit shown in the TEM image of Figure 5.3(b). In the GaAs bulk region (left-hand side of the image in Figure 5.3(b)), the Ga and As counts are nearly equal indicating the stoichiometric composition of GaAs. As the linescan proceeded across the pit toward the sample surface, the As composition clearly increased and the Ga composition decreased, indicating an As-rich composition in the pit region. Finally, as the linescan proceeded toward the sample surface, the O composition increased, indicating the presence of the UV-ozone oxide. The Ga composition increased relative to the As composition, indicating a UV-ozone oxide comprised primarily of Ga oxides. Therefore, the UV-ozone oxide, after annealing, was rich in Ga and the pit was rich in As for the GaAs (100) surface. A model consistent with these results will be presented in section 5.4.
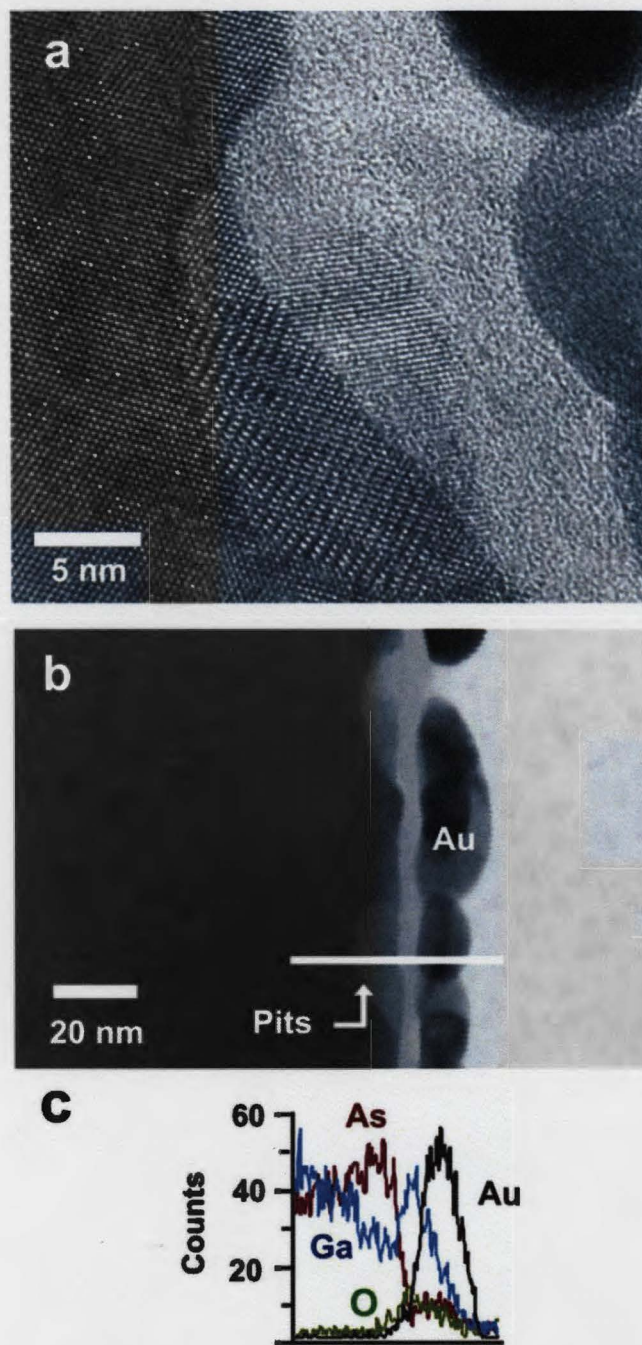
Figure 5.3. (a) HRTEM image viewed along the [011] direction showing a pit on the surface of a UV-ozone oxidized GaAs (100) substrate (treatment B) after the formation of Au particles by annealing at 500 °C for 300 s. (b) TEM image showing location of EDXS linescan (white line) across a pit. (c) EDS linescan across the pit in (b) showing counts of Ga (blue), As (red), O (green), and Au (black).

Next, the influence of the various surface treatments on the density and growth direction of nanowires was examined. Plan view SEM images shown in Figure 5.4 and cross-sectional SEM images (not shown) indicated that the majority of nanowires grew along the energetically favorable <111>B direction for all three surface treatments. However, nanowires were also observed to grow along other directions, namely the <011>, <111>, <110>, <211>, <411>, <511> and <100> directions making angles of 0°, 35.3°, 45°, 54.7°, 70.5°, 74.2° and 90°, respectively, relative to the substrate surface. In addition, the surface density of nanowires and the relative abundance of the different growth directions were dependent on the surface treatment as summarized in Table 5.1.
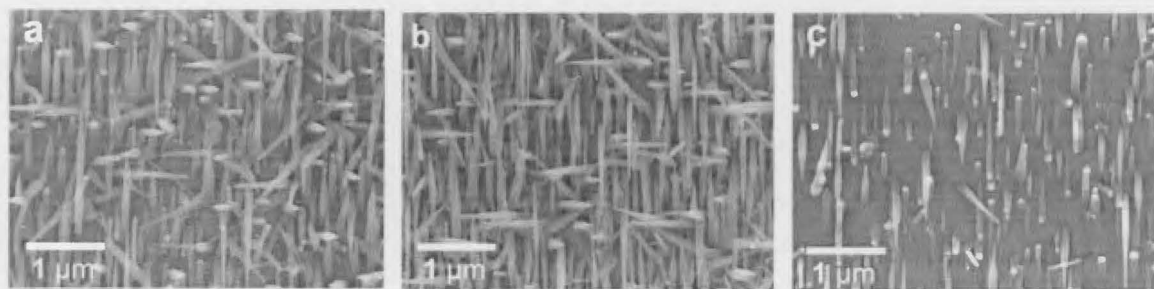
Figure 5.4. Plan view SEM images of nanowires grown on GaAs (100) surfaces after (a) treatment A (Epi-ready), (b) treatment B (UV-ozone oxidized), and (c) treatment C (UV-ozone/HF etch).

Most notably, the A- and B-treated surfaces resulted in a surface density of nanowires which was about 75% greater than the C-treated surface. In addition, although the <011> nanowires (lying parallel to the substrate surface) encompassed a large fraction of the total nanowire population on the C-treated substrate, no such nanowires were found to grow on either the A- or the B-treated substrates.

Regardless of the surface treatment, the nanowire density was at least two orders of magnitude lower than the initial density of Au particles measured after thermal annealing and plasma cleaning. More specifically, the ratio of Au particle density to nanowire density for the A-, B-, and C-treated surfaces was 140, 367, and 104, respectively.

Table 5.1. Abundance of nanowires growing along different crystallographic directions, depending on surface processing of the GaAs (100) substrate. Angles corresponding to each growth direction, defined relative to the substrate surface, are indicated in parentheses.

Treatment	Density of Nanowires (cm^{-2})	Nanowire growth direction						
		<011> (0°)	<111> (35.3°)	<110> (45°)	<211> (54.7°)	<411> (70.5°)	<511> (74.2)	<100> (90°)
A	1.5×10^9	-	71.5%	7.6%	7.0%	13.9%	-	-
B	1.5×10^9	-	77.6%	5.7%	7.7%	9.0%	-	-
C	8.5×10^8	45.3%	46.4%	0.9%	1.3%	-	4.2%	1.9%

To further examine the disparity between Au nanoparticle and nanowire densities, the C-treated substrate was examined more closely at various intervals of the nanowire growth process. As shown in Figure 5.5, a decreasing trend of surface density was observed at every stage of growth. A large change in density from the as-deposited Au was found after thermal annealing and plasma cleaning in the MBE chamber when Au clusters agglomerate to form larger particles. Furthermore, when subjected to growth, not all the catalytic particles were able to nucleate nanowires, and a large portion of nanowires became buried within the 2-D film growing simultaneously between the nanowires.

Figure 5.6, for example, shows numerous Au nanoparticles and nanowires buried within the 2-D film.
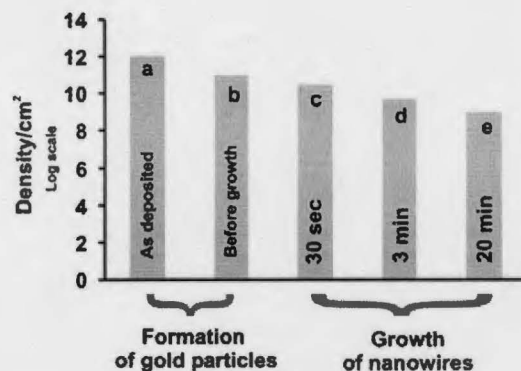
Figure 5.5. Surface densities of Au nanoparticles and GaAs nanowires on the HF-treated GaAs (100) substrate for treatment C. (a) As-deposited Au; (b) Au after thermal annealing and plasma cleaning in the MBE chamber; and nanowires after (c) 30 s, (d) 3 min, and (e) 20 min growth durations.
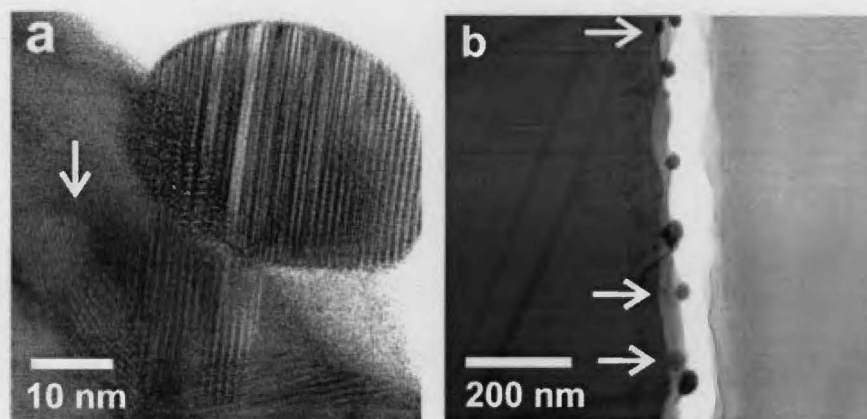
Figure 5.6. HRTEM image viewed along the [011] direction for C-treated GaAs (100) sample, showing (a) a nanowire buried after 2 min. of growth (indicated by arrow) and (b) gold seed particles buried after 3 min of growth (indicated by several arrows).

To understand the origin of the nanowire growth directions, cross-sectional HRTEM was performed with an emphasis on the most abundant <011> and <111>B nanowires. Figure 5.7(a) shows a TEM image of an interface region between the single gold nanoparticle and the underlying GaAs after a growth duration of 1 min on a C-treated surface.
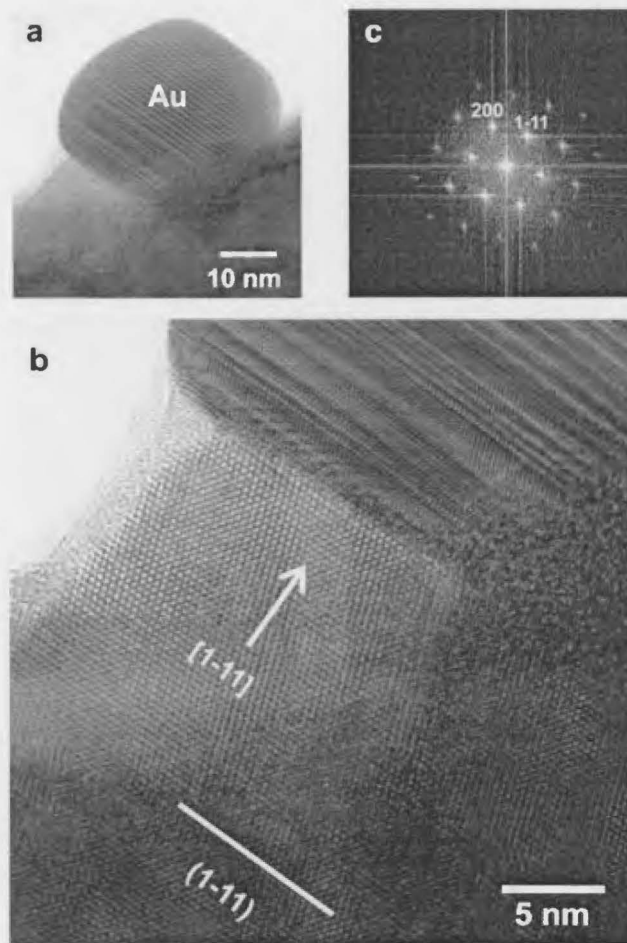
Figure 5.7. HRTEM image of [1-11] directed nanowire viewed along the [011] direction under (a) low magnification, and (b) high magnification. The (1-11) facet of the surface pit, and [1-11] growth direction of the nanowire are indicated. (c) FFT of the nanowire region for the image in (b).

The planar Au-GaAs interface is perpendicular to the [1-11] direction, indicating that the Au nanoparticle nucleated from (111)B planes. Furthermore, a Fast Fourier Transform (FFT) of the GaAs region beneath the Au particle, shown in Figure 5.6(c), revealed a zincblende crystal structure with a lattice spacing of 3.25 Å along the growth direction corresponding to the GaAs(111) interplanar spacing. Close inspection of the base region of the short nanowire in Figure 5.7(b), as well as other similar <111>B nanowires, revealed that the {111}B GaAs planes appear to nucleate from the {111}B sidewalls of the surface pits. We therefore speculate that the nucleation of <111>B oriented nanowires occurs due to gold particles originally situated in the surface pits.
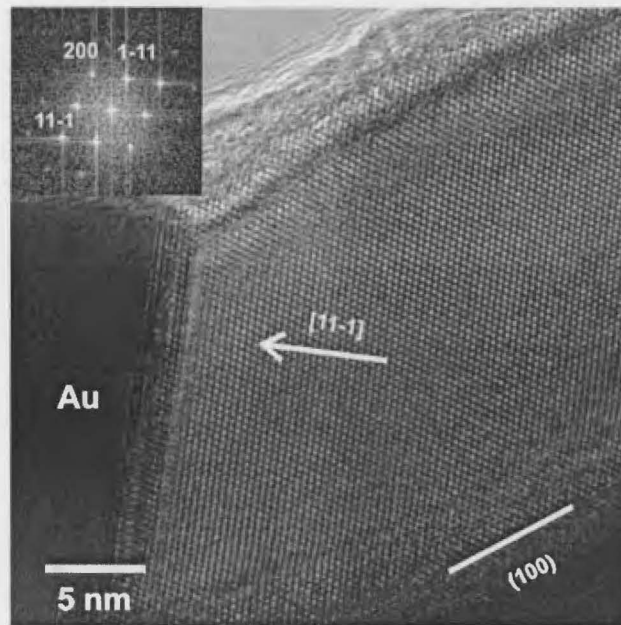
Figure 5.8. HRTEM image showing a [01-1] nanowire on the GaAs (100) substrate viewed along the [011] direction. The (100) planes of the GaAs substrate and the [1 1 -1] direction are indicated. Inset is the FFT of the image showing zincblende crystal structure.

Next, we examined the nanowires growing along the [0 1 -1] and [0 -1 1] directions, parallel to the C-treated surface. Cross-sectional HRTEM did not show the presence of any pits near these nanowires. Rather, they appeared to originate from the Au seed particles present on the non-pitted areas of the substrate. For example, Figure 5.8 shows a [0 1-1] oriented nanowire growing along the (100) surface plane for a 3 minute growth duration. FFT analysis (inset of Figure 5.8) indicated that the nanowires had zincblende crystal structure similar to the <111>B nanowires considered earlier. The Au-nanowire interface was perpendicular to the (1 1 -1) planes of the nanowire. The latter observation indicates that the Au particle remained on the substrate surface, while nucleating (1 1 -1) planes at the Au-nanowire interface.

5.3 Discussion

5.3.1 Pit formation

Figure 5.1 revealed that pits having varying dimensions and orientation appeared on GaAs (100) substrates depending on surface preparation prior to growth. B-treated GaAs (100) substrates that underwent UV-ozone oxidation were found to be severely pitted after thermal annealing (Figure 5.3) and after plasma cleaning (Figure 5.1(b)). Pits begin to form on the GaAs (100) substrate during UV-ozone oxidation in which the photo-chemically generated atomic oxygen reacts with the GaAs surface. The oxygen atoms initially insert into the arsenic-gallium backbonds by dislodging arsenic atoms in the top dimer rows and becoming chemisorbed into the arsenic sites underneath [57]. If this reaction is continued, the pits are formed and become elongated along [01-1]

directions on the GaAs (100) substrate. The dislodged As atoms form metallic clusters at the interface. The oxide layer thus formed, as discussed in section 2.1, on GaAs after 20 minutes of UV-ozone oxidation has a thickness of approximately 3.5 nm and shows a rather complex chemical composition consisting of $-As_xGa_2O$, Ga_2O3, As_2O_5 and $Ga(OH)_3$ in addition to having elemental As and As_2O_3 [42]. Annealing the UV-ozone oxidized GaAs has the effect of complete desorption of $Ga(OH)_3$ and As_2O_5, and partial desorption of As_2O_3 and $-As_xGa_2O$ making the oxide layer rich in Ga. However, As_2O_3 near the substrate interface can react with the bulk according to the following solid state chemical reaction:

$$As_2O_3 + 2GaAs \rightarrow Ga_2O_3 + 4As \qquad \text{Eq. 5.1}$$
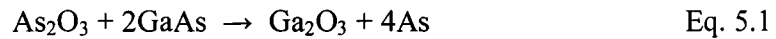
that results in the formation of elemental As at the interface. Moreover, Ga_2O_3 reacts with Ga to form Ga_2O in order to desorb according to the reaction [91, 93]

$$Ga_2O_3 + 4Ga \rightarrow 3Ga_2O \qquad \text{Eq. 5.2}$$

During the annealing, formation of As_2 is thermodynamically possible and it can either leave the system or be trapped within the oxide layer [43]. The pit region therefore becomes rich in As with an overlayer of Ga-rich oxide as confirmed by the EDS in Figure 5.3(c). The As-rich pit region can be considered as an inclusion of another phase of material at the oxide-substrate interface due to the occupancy of undesorbed As in the vacant Ga sites which forms a local region of antisite As defects while retaining the cubic symmetry of the bulk [94].

In the case of C-treated surfaces, the UV-ozone oxide was removed by HF etching prior to the Au deposition. After thermal annealing and plasma cleaning of the C–treated

GaAs (100) substrate, pits were found to grow in a direction perpendicular to those formed by the UV-ozone oxide described above for treatment B. In this case, we propose that the pit formation results from interaction of Au with the GaAs surface. At the oxide desorption temperature of 500 °C, according to the Au-Ga phase diagram [95], solubility of Ga in Au is as high as 20%. As a result, highly mobile Au clusters react with Ga and this dissolution of Ga is continued until the Au particles reach thermodynamic equilibrium. The GaAs (100) surface consists of highly anisotropic terraces having bi-layer steps with the long steps lying along [0 1 -1] and short steps along [011] directions. The long steps are Ga-faced and the short steps are As-faced planes. Gold acts as an 'etchant' for Ga and, consequently, the Ga-faced planes will react faster than As-faced planes resulting in pits elongated along the [011] direction, consistent with previous observations [92].

Finally, treatment A consisted of Au deposition directly on the Epi-ready GaAs (100) substrate. The Epi-ready surface includes a native oxide ~1 nm thick. The presence of this oxide, albeit thinner than the UV-ozone oxide, might be expected to produce surface pits similar to those observed for treatment B. However, thermal annealing and plasma cleaning of the Epi-ready surfaces resulted in pits that were elongated along the [011] direction, similar to the HF-etched surface of treatment C. It therefore appears that the dominant effect in the Epi-ready samples is the interaction of the Au with the substrate surface rather than the interaction of the oxide. This might be explained by the smaller thickness and composition of the Epi-ready oxide, which is more easily desorbed, leaving less interaction of the oxide with the sample surface.

5.3.2 Density of Au Nanoparticles and Nanowires

Both the size distribution and areal density of particles were dependent on the surface treatment. B-treated substrates resulted in particles having the lowest average size, whereas the largest particles were found on C-treated substrates. According to our previous studies [41], this difference can be attributed to the change in "wetting" properties of the Au nanoparticles on the substrate surface induced by the surface preparation. Since the surface energy of Au is higher than that of oxidized GaAs, Au has a natural tendency to form nanoparticles on the oxide surface [19]. Annealing has the effect of reducing the density of islands by 'Ostwald ripening' or by 'coalescence' in which small clusters are mobile and combine to form larger islands. However, nucleation of metal clusters on oxide surfaces is known to be dominated by defect sites [96] and island size distribution is, therefore, controlled by spatial distribution of defects when the diffusion length is comparable with or greater than the distance between defect traps [97]. This implies that, assuming that the diffusion length of gold is greater than the defect trap separation, the slightly higher density of catalytic particles on the B-treated substrate is due to the presence of higher defect density on UV-Ozone oxide than that on the epi-ready wafer surface of treatment A. In the case of C-treated substrates, pits are formed from the UV-ozone process as in treatment B. However, the UV-ozone oxide in treatment C was removed prior to Au deposition and Au was deposited directly onto the pitted GaAs surface. Our previous results showed that the pits appeared to act as nucleation centers by effectively 'collecting' the deposited Au. As a result, island size distribution on C-treated GaAs (100) substrates spanned a broad range with an increase in average

size along with a decrease in the density of catalytic particles in comparison to A- and B-treated substrates [41].

The increased density of nanowires on A- and B-treated substrates is correlated to the greater Au particle density that was observed on the oxide-covered surfaces of treatments A (native oxide) and B (UV-ozone oxide). However, as shown in Figure 5.5, the density of nanowires decreased as the growth progressed and the nanowire density was lower than the as-deposited Au particle density. First, significant agglomeration of the Au nanoparticles can be expected through Oswald ripening and coalescence of particles. Second, nanoparticles less than a certain critical size will not nucleate nanowires due to the Gibbs-Thomson effect [98, 99]. This effect is particularly relevant to the oxide-covered surfaces of treatments A and B which exhibited the smallest Au particles. The decrease in density of nanowires was therefore greatest for the A- and B-treated surfaces. Finally, a large fraction of nanowires become buried under the 2-D film growing simultaneously between the nanowires as shown in Figure 5.6.

5.3.3. Nanowire Growth Direction

As shown in Table 5.1, both the density and orientation of nanowires were strongly influenced by the surface preparation prior to Au deposition. Irrespective of surface preparation, the majority of nanowires grew along the energetically favorable <111>B directions. The origin of these nanowires was suggested by the TEM analysis of Figure 5.7, which indicated that the nanowires growing along the <111>B directions nucleated on either the (1-11) or (11-1) facets of the pits. The lower density of <111>

nanowires on the C-treated surface, compared to A- and B-treated surfaces, can then be explained by the lower density of pits associated with treatment C.

A large portion of nanowires on the C-treated substrates were lying flat on the surface, i.e. growing along the [01-1] and [0-11] directions. The TEM analysis of Figure 5.8 revealed that these nanowires originated from Au particles situated on non-pitted regions of the substrate which are far more abundant on the C-treated surface as compared to the A- or B-treated surfaces. As a result, Ga adatoms incorporate into the Au particle by diffusing on the substrate surface which occurs preferentially along the [01-1] direction on GaAs (100) where a lower energy barrier to diffusion exists [100]. Glas *et al* [101] have shown that nucleation takes place preferentially along the triple phase boundary at the Au-nanowire or Au-substrate interface. Nucleation might be expected to occur preferentially along the direction of adatom diffusion, i.e., along [01-1] or [0-11] directions.

5.4 Chapter Summary

In conclusion, we have verified that both density and orientation of nanowires are strongly influenced by the topography of the GaAs (100) substrate prior to growth. The change in topography is due to the formation of pits of various size and orientation due to the interaction of gold and oxide with the GaAs surface. Change in surface processing not only changed the surface topography, but also affected the Au particle density and size distribution. The orientation of nanowires along the <111>B direction resulted from nucleation on the B-faced planes of the pit sidewalls, while the [011] type nanowires

resulted from Au particles situated on non-pitted areas of the substrate surface. The

crystallographic features of nanowires along other growth directions will be discussed in

the next chapter.

Chapter 6

Control of Growth Directions of Nanowires

In this chapter, we discuss the routes of controlling the growth directions of nanowires on GaAs (100) substrates. The growth directions of nanowires can be significantly altered by changing growth rate as well as distribution of seed particles prior to growth. Moreover, orientation-dependent crystallographic properties of nanowires have been analyzed and discussed in relation to their initiation of growth.

6.1 Experimental Details

Prior to growth of the nanowires, n-type GaAs (100) Epiready wafers (supplied by Wafer Technology Ltd.) underwent a UV ozone oxidation for 20 minutes, followed by etching with buffered hydrofluoric acid for 30 sec, to remove hydrocarbons. Deposition of 5, 10 and 14 Å of Au occurred at room temperature by e-beam evaporation and measured using a quartz crystal thickness monitor. The sample was subsequently transported in ambient air to the gas source molecular beam epitaxy (MBE) chamber for nanowire growth. Group III monomers (Ga) were supplied from a solid elemental effusion cell and Group V dimers (As_2) were supplied from a hydride (AsH_3) gas cracker operating at 950 °C. After annealing at 500 °C for 5 minutes, an *in-situ* inductively coupled H_2 plasma treatment at 550 °C for 10 minutes was used to remove surface oxide under a group V overpressure. The growth of nanowires was initiated by opening the Ga shutter at 2-D growth rates of 1.0, 0.5 and 0.25 μm/hr (equivalent to 1, 0.5 and 0.25 ML/sec, respectively) for 10, 20 and 40 minutes, respectively, such that all samples received an identical material supply. The substrate temperature was 500 °C for all samples, and the V/III flux ratio was 1.5 for 1 ML/sec samples, and 3.0 for 0.5 ML/sec and 0.25 ML/sec samples, as summarized in Table 6.1.

Growth was terminated by closing the Ga shutter and cooling down under an As_2 overpressure. Samples were examined by a JEOL JSM-7000F field emission scanning electron microscope (SEM), a JEOL JEM-2010F high resolution transmission electron microscope (HRTEM), and a Philips CM12 transmission electron microscope (TEM). Thin foils for TEM were prepared by mechanical thinning and Ar ion beam milling, or

thin lamellae were prepared by focused ion beam milling using a LEO 1540XB and a

Zeiss N-Vision 40 instrument.

Table 6.1 Summary of samples used in the study

Sample	Gold Thickness (Å)	2-D Equivalent Growth Rate (ML/sec)	Growth Duration (min)	V/III Flux Ratio
A		1.00	10	1.5
B	5	0.50	20	3.0
C		0.25	40	3.0
D		1.00	10	1.5
E	10	0.50	20	3.0
F		0.25	40	3.0
G	14	1.00	10	1.5
H		0.50	20	3.0

6.2 Results

The surface densities of nanowires were calculated by taking plan-view SEM

images at the same magnification from different areas of each sample. Irrespective of

initial gold thickness, the surface density of nanowires was found to increase with the 2D

equivalent growth rate, as shown in Figure 6.1.

The orientation of the nanowires was also found to be dependent on the growth

rate as well as seed particle distribution prior to growth. Nanowires on GaAs (100)

substrates grow along a number of crystallographic directions [33, 44]. In this Chapter,

our discussion will be focused on <011> and <111> oriented nanowires that constitute
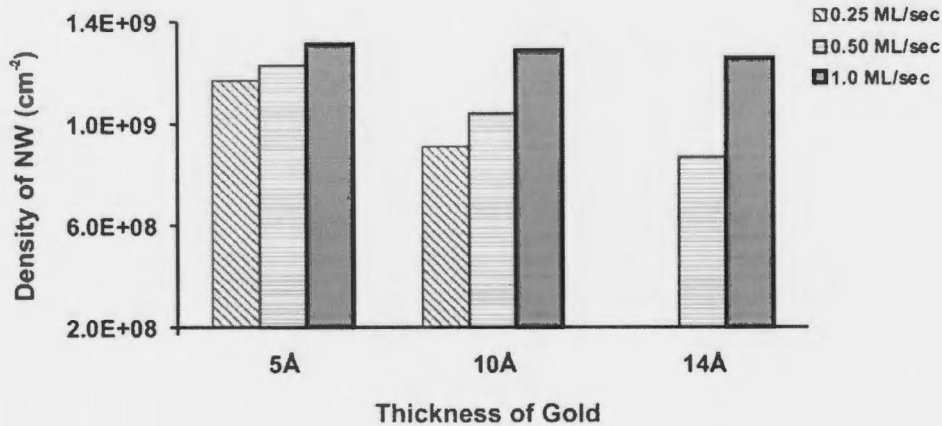
Figure 6.1. Surface densities of nanowires grown by MBE at 500°C at different growth rates for time periods equivalent to a 2D thickness of 167 nm. Irrespective of initial gold thickness, the density of nanowires increases with growth rate.

more than 90% of the nanowires, grown at a nominal growth rate of 1.0 ML/sec at 500 °C. As shown in Figure 6.2(a), for a particular gold thickness, the relative distribution of <011> and <111> directed nanowires varied significantly with growth rate. At lower growth rate, the density of <011> oriented nanowires decreased coincident with an increase of <111> nanowires. The surface density of <111> oriented nanowires was maximized at a growth rate of 0.5 ML/sec for all gold thicknesses examined in this study.

The growth of nanowires by MBE is accompanied by a 2-D film growth on the substrate. The thickness of the 2-D layer was measured from cross-sectional TEM images of the samples. As shown in Figure 6.2(b), the thickness of this layer did not increase linearly with growth rate; rather it attained a minimum value at an intermediate growth rate of 0.5 ML/sec (sample E), and higher values at 0.25 ML/sec (sample F) and 1.0 ML/sec (sample D). This suggests that the surface density of <111> oriented nanowires is maximized when the film growth rate is minimized as discussed further below.
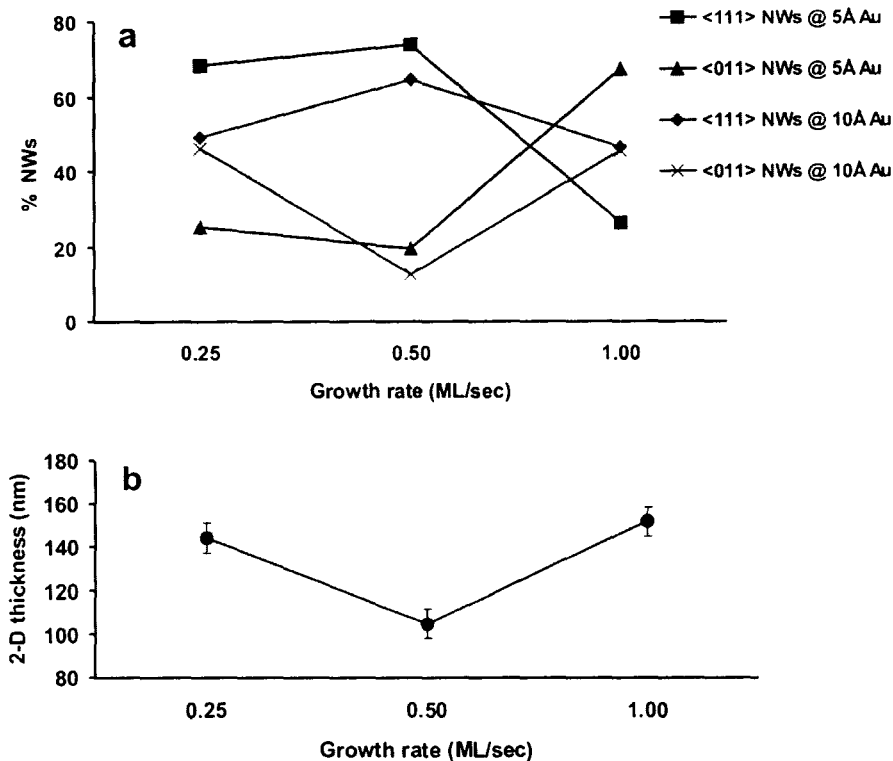
Figure 6.2. Effect of growth rate on (a) the orientation of nanowires (only <110> and <111> directed nanowires are shown) on GaAs (100) substrates grown from 5Å and 10Å of gold. (b) The thickness of 2-D layers, measured from cross-sectional TEM images, obtained during nanowire growth for 10Å of gold. Error bars refer to the standard deviation in thickness measurements from TEM images. Lines are guides to the eye.

Apart from the effect of growth rate, seed particle distribution prior to growth was also found to be crucial to determining the growth direction of nanowires. As mentioned in the last chapter, formation of seed particles is accompanied by a change in surface topography and the seed particles were found to be dispersed both on pitted and non-pitted regions on the surface. Statistical analysis of seed particle size distribution (by ImageJ software), evolving from 1 nm of gold (C-treated substrate of Chapter 5) prior to

nanowire growth exhibited nearly Gaussian distributions in both areas with an average

size larger in pitted areas in comparison to non-pitted areas of the sample, as shown in

Figure 6.3.
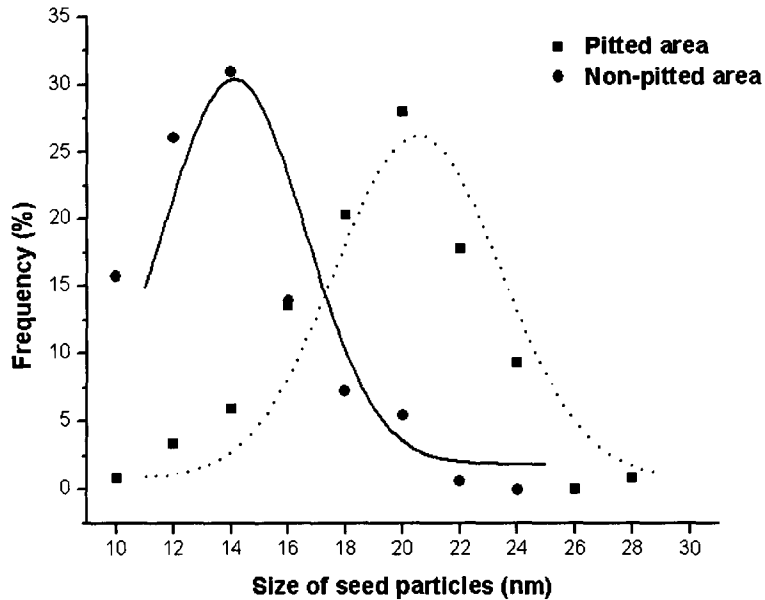
Figure 6.3. Seed particle distribution in the pitted (dotted line) and non-pitted area (solid line) on GaAs (100) substrate prior to initiation of nanowire growth.

SEM images of nanowires, as shown in Figure 6.4, illustrate the dependence of

nanowire orientation on gold thickness. Analysis of the SEM images allowed us to

calculate the relative abundance of nanowires based on their orientations. As shown in

Figure 6.5, for a growth rate of 0.5 ML/sec, the distribution of <111> nanowires

decreased with gold thickness (samples B, E and G), but this change was drastic when the

thickness was changed from 10 Å to 14 Å - the distribution of <011> nanowires

increased coincident with a decrease in <111> oriented nanowires. Interestingly, the

presence of about 8% [100] oriented nanowires (vertical nanowires) were found to grow

on samples E and G.
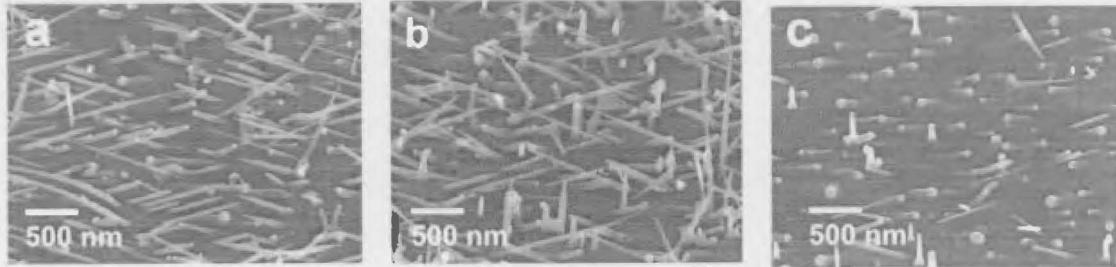
Figure 6.4. Effect of gold thickness on the growth direction of nanowires on GaAs (100) substrates. Nanowires were grown at the rate of 0.5 ML/sec at 500 °C with a V/III flux ratio of 1.5 from seed particles arising from gold films of (a) 5 Å (b) 10 Å and (c) 14 Å thickness.
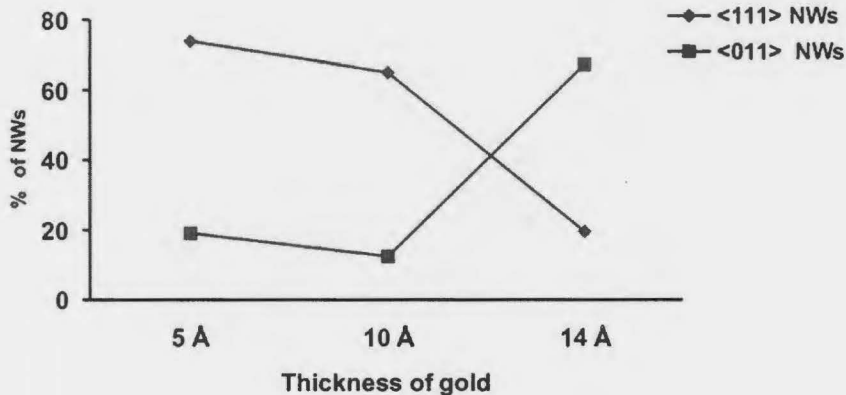
Figure 6.5. Effect of gold thickness on the orientation of nanowires grown on GaAs (100) substrates at 500 °C at a growth rate of 0.5 ML/sec. The distribution of <111> NWs decreases drastically coincident with an increase in <011> NWs as the gold thickness was increased from 10Å to 14Å. Lines are guides to the eye.

Next, we analyzed the orientation-dependent crystallographic properties of the

nanowires. The <111> oriented nanowires were found to contain periodic arrays of

stacking faults perpendicular to the growth direction. Fast Fourier Transforms (FFT) on

HRTEM images, as shown in Figure 6.6, produced a set of spots similar to the diffraction

pattern of the hexagonal close-packed crystal structure along the [2-1-10] zone axis, indicating that the nanowire grew along <0001> direction with wurtzite crystal structure. Analysis of HRTEM images along the growth direction showed that the nanowire maintained a stacking sequence of ABABAB.... having a lattice spacing of 3.29Å, as expected for (0002) inter-planar spacing of wurtzite GaAs crystals [102].
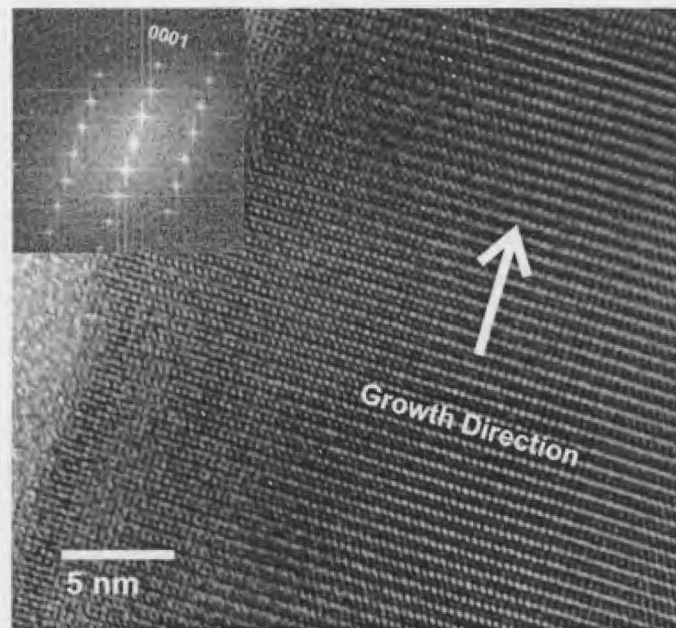
Figure 6.6.   HRTEM image of a <111> oriented nanowire grown on GaAs (100) substrate. Fast Fourier Transformation (FFT) in the inset corresponds to the [2-1-10] zone axis of hexagonal close-packed crystal structure and reveals that the nanowire has wurtzite crystal structure.
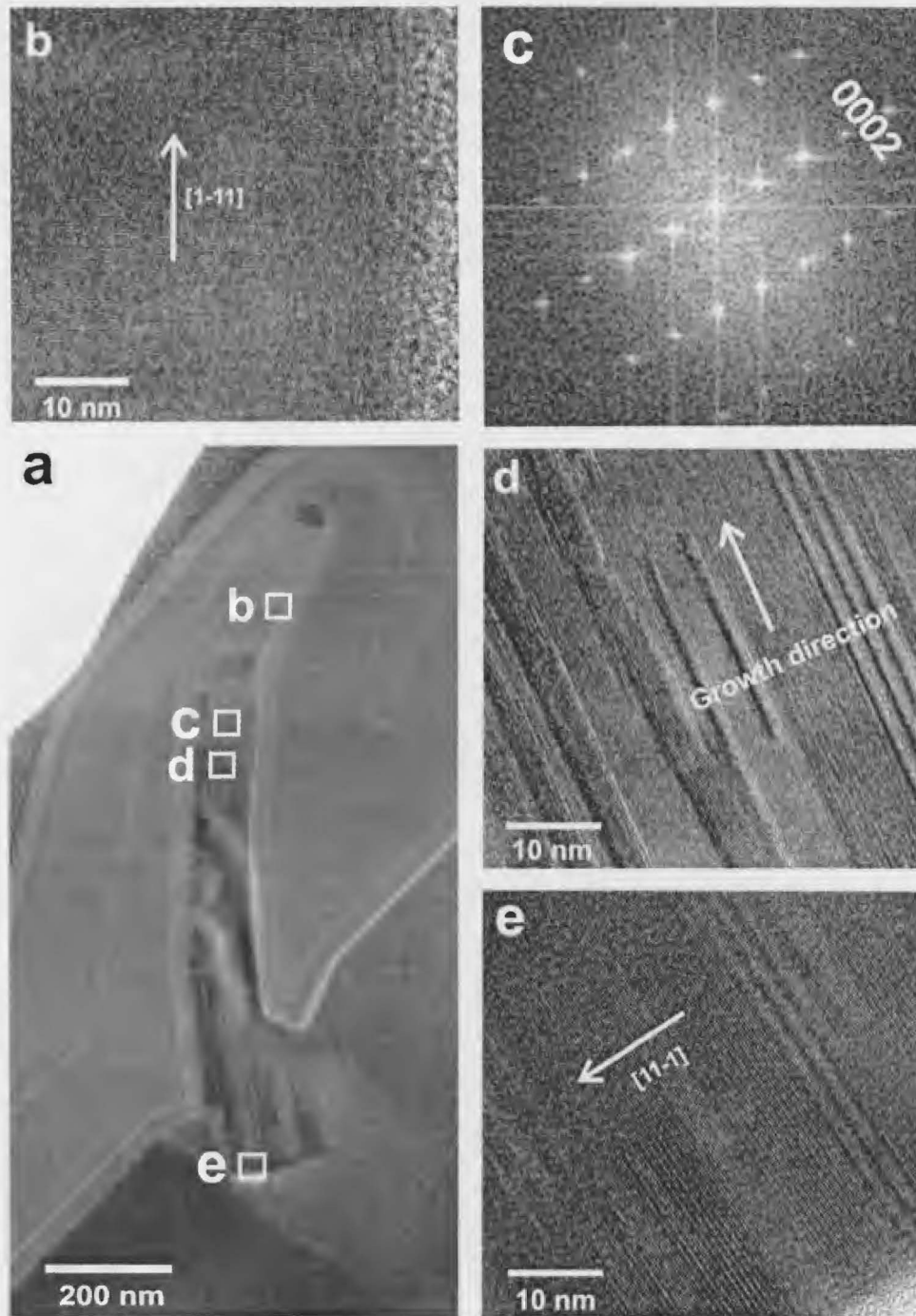
Figure 6.7. (a) TEM image of a [2-11] nanowire viewed along the [011] direction. HRTEM images near (b) the nanowire top, (d) the body of the nanowire below the kink and (e) at the nanowire base. (c) Fast Fourier Transformation (FFT) of the nanowire in the region labeled c of (a) reveals that the nanowire has wurtzite crystal structure.
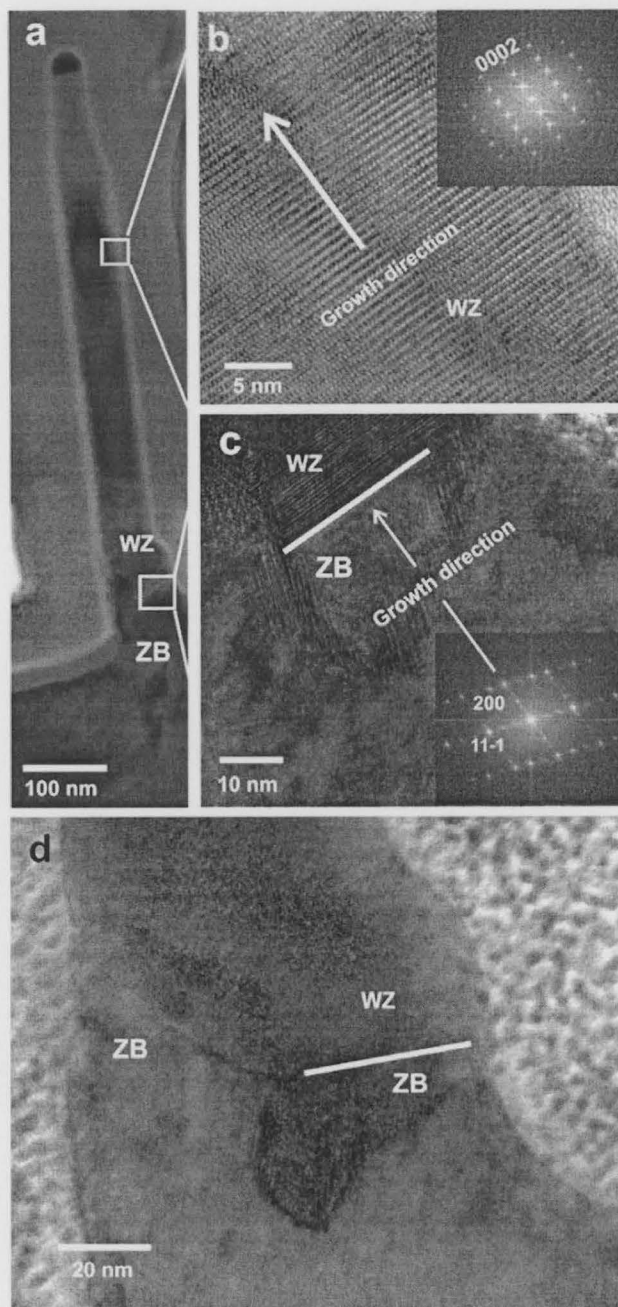
Figure 6.8. (a) TEM image of a [5-11] nanowire viewed along the [0-11] direction. (b) HRTEM near the nanowire top. Inset shows FFT of image. (c) HRTEM near the nanowire base. Inset shows FFT of image. Line indicates the transition from zincblende to wurtzite crystal structure. (d) TEM showing transition region between zincblende (ZB) and wurtzite (WZ).

Analysis of the <211> oriented nanowire, as shown in Figure 6.7, showed that the nanowire has wurtzite crystal structure having (111) planes parallel to the growth direction and contained a series of stacking faults parallel to the growth direction. After kinking, the nanowire grew along the <111> direction.

Next, we analyzed the crystallographic properties of <511> directed nanowires, the near-vertical nanowires growing at 74.2° relative to the substrate (Figure 6.8). These nanowires appeared to have zincblende crystal structure at the initial stage and suddenly transitioned to a wurtzite crystal structure coincident with a change in growth direction.
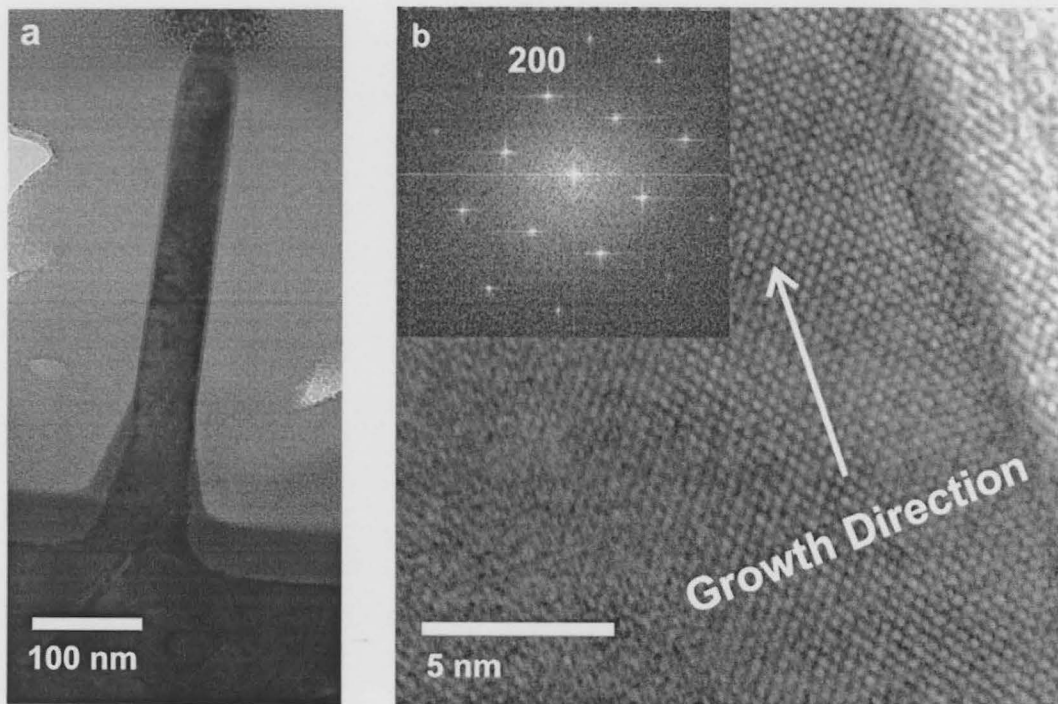
Figure 6.9. TEM images of a [100] oriented nanowire, as viewed along [011] direction with (a) low resolution, and (b) high resolution. FFT in the inset confirms the zincblende crystal structure of the nanowire.

Lastly, the crystal structure of [100] nanowires was analyzed. As shown in Figure 6.9, unlike <111> nanowires, the <100> directed nanowires had zincblende crystal structure, as confirmed by FFT (shown in inset). After taking a number of images from different areas, these nanowires appeared to be defect-free, which was further confirmed by imaging along [012] and [0 -11] directions.

6.3 Discussion

6.3.1 Effect of Growth Rate on Nanowire Surface Density

The surface density of nanowires was found to increase with growth rate irrespective of initial thickness of gold. For identical distribution of gold seed particles, the increase in density with increasing growth rate (impingement flux) could possibly be attributed to the Gibbs-Thomson effect, which, in the case of nanowire growth, determines the net arrival-rate of adatoms towards the growth interface, R [25]:

$$R = \frac{P - P_\infty \exp(2\sigma\Omega_l / r_w k_B T)}{\sqrt{2\pi m k_B T}}$$

Eq. 6.1

where the first term on the right-hand side describes the group III pressure surrounding the seed particle and the second term describes the equilibrium pressure with decreasing size due to the Gibbs-Thomson effect; P_∞ is the Ga pressure inside a large gold seed particle and other parameters have the same meanings as described in section 1.0. In the case of nanowire growth in MBE, the higher growth rate implies more group III atoms in

the gas phase, which increases the ambient pressure surrounding the seed particles. As a result, more seed particles take part in the growth process and the surface density of nanowires increases with growth rate, consistent with previous observation [103].

6.3.2 Effect of Growth Rate on Nanowire Growth Direction

The 2-D layer thickness showed a minimum at intermediate growth rates as shown in Fig. 6.2(b). Adatoms adsorbed onto the substrate will incorporate either into the Au seed particles or the 2-D layer. At high growth rates (1.0 ML/s), the diffusion of adatoms may be kinetically limited, meaning that adatoms may incorporate and be covered over by the 2-D film rather than diffuse to seed particles for nanowire growth. On the other hand, if the growth rate is low (0.25 ML/s), the Gibbs-Thomson effect may inhibit the incorporation of adatoms into the seed particles, and the growth of a 2-D layer is again favored. As a result of these two processes, the rate of incorporation of adatoms into the seed particles, i.e., the 'nanowire growth-rate' is maximized at the intermediate growth rate (0.5 ML/s) where the 2-D film thickness is minimized. This observation is consistent with the theoretical calculation of nanowire growth-rate reaching a maximum value for an intermediate growth rate of 0.5-0.6 ML/sec [103].

At this point, it is worth discussing the effect of changing V/III flux ratio on the growth rate of nanowires. As mentioned earlier, nanowires, in this study, were grown at 500 °C at a growth rate of 1.0 ML/sec with a V/III flux ratio of 1.5, and at growth rates of 0.5 and 0.25 ML/sec with a V/III flux ratio of 3.0. The implication of reduced diffusion length of Ga as a result of increased As pressure, as observed during growth on planar GaAs (100) substrates by MBE [104], has been found to be negligible in the growth of

nanowires. It has been demonstrated that, above a certain V/III molar ratio, the nanowire growth rate in MOCVD is independent of the group V precursor concentration, while it is linearly dependent of the group III precursor concentration [105]. Similar work in MBE by Plante *et al* [35] has revealed that the nanowire growth rate at 500 °C is not strongly affected by a change in V/III flux ratio from 1.7 to 2.3 for a growth rate of 1.0 ML/sec. These observations imply that as long as the V/III flux ratio at the particle-nanowire interface is more than unity, the growth-rate of nanowires will primarily be determined by the impingement rate of the group III material, not by the V/III flux ratios. Since nanowires in this study were grown at 500 °C with V/III flux ratios much higher than unity, it is therefore reasonable to assume that changes in V/III flux ratios have no significant effect on the growth rate of nanowires.

6.3.3 Effect of Au Thickness on Nanowire Growth Direction

Changing the thickness of gold also affects the orientation of nanowires on a GaAs (100) substrate, as shown in Fig. 6.5, with thicker Au films favoring <011> nanowires. As we reported earlier [41], increasing the initial gold thickness has the effect of skewing the particle size distribution to larger particle diameters. To determine the size-dependent 'incubation time', defined as the time required for seed particles to become saturated for the initiation of nanowire growth, we will use a simple model developed by Dubrovskii [106]. When Ga adatoms are supplied in the vapour phase by opening the Ga shutter, the seed particle will try to accumulate Ga until a thermodynamic equilibrium is reached. To determine the number of Ga atoms (N_{Ga}) accumulated in the

seed particle at a given time, we need to consider different pathways of Ga adatom

incorporation into the gold particle. Assuming that the seed particle is hemispherical

having a radius r, the accumulation of atoms can occur along the following pathways:

1. Adsorption of Ga adatoms directly on the particle:

$$J_{ads} = \pi r^2 \times x \Big/ \Omega_{Ga}$$

Eq. 6.2

where x is the impingement rate in ML/sec and Ω_{Ga} is the atomic volume.

2. Adatoms impinging on the substrate will diffuse to the catalyst particle. The amount

    of adatom incorporation to the particle will be proportional to the difference in

    impingement rate x and 2-D growth rate (x_{2D}) on the substrate. Since the rate of

    adatoms being intercepted by a particle is proportional to the perimeter of the

    particle, the flux of adatoms being incorporated through surface diffusion can be

    written as [106]:

$$J_{diff} = \frac{r}{<r> \times P_{particle}} \times \frac{x - x_{2D}}{\Omega_{Ga}}$$

Eq. 6.3

where <r> is the mean radius of particles, and $P_{particle}$ is the density of seed particles.

Combining the above two equations gives us the rate of Ga accumulation in the particle:

$$\frac{dN_{Ga}}{dt} = \pi r^2 \times \frac{x}{\Omega_{Ga}} + \frac{r}{<r> \times P_{particle}} \times \frac{x - x_{2d}}{\Omega_{Ga}}$$

Eq. 6.4

with the boundary condition of $N_{Ga} = N_0$ at t = 0. Consider that at a time t, the particle

will reach its equilibrium concentration N_{eq}. Integrating the above equation gives:

$$N_{eq} - N_0 = (\pi r^2 \times \frac{x}{\Omega_{Ga}} + \frac{r}{<r> \times P_{particle}} \times \frac{x - x_{2d}}{\Omega_{Ga}})t$$

Eq. 6.5

For a specific size distribution $<r>$ and $P_{particle}$ remain unchanged and Ω_{Ga} is constant. As a result, the incubation time for any size of seed particle will primarily be determined by different growth rates (x, x_{2d}). Assuming $N_0 = 0$, we can roughly estimate the incubation time depending on growth rate and seed particle distribution. At a growth temperature of 500 °C, the equilibrium concentration of Ga is about 20 atomic percent [95], which after incorporating in Eq. 6.4, gives us:

$$\frac{2}{3}\pi r^3 \times 0.2 \times \frac{1}{\Omega_{Au}} = (\pi r^2 \times \frac{x}{\Omega_{Ga}} + \frac{r}{<r> \times P_{particle}} \times \frac{x - x_{2d}}{\Omega_{Ga}})t \qquad \text{Eq. 6.6}$$

Assuming $\Omega_{Au} \cong \Omega_{Ga}$, the equation can be rearranged as:

$$t = \frac{0.419r^2}{3.14rx + \dfrac{x - x_{2d}}{<r> \times P_{particle}}} \qquad \text{Eq. 6.7}$$
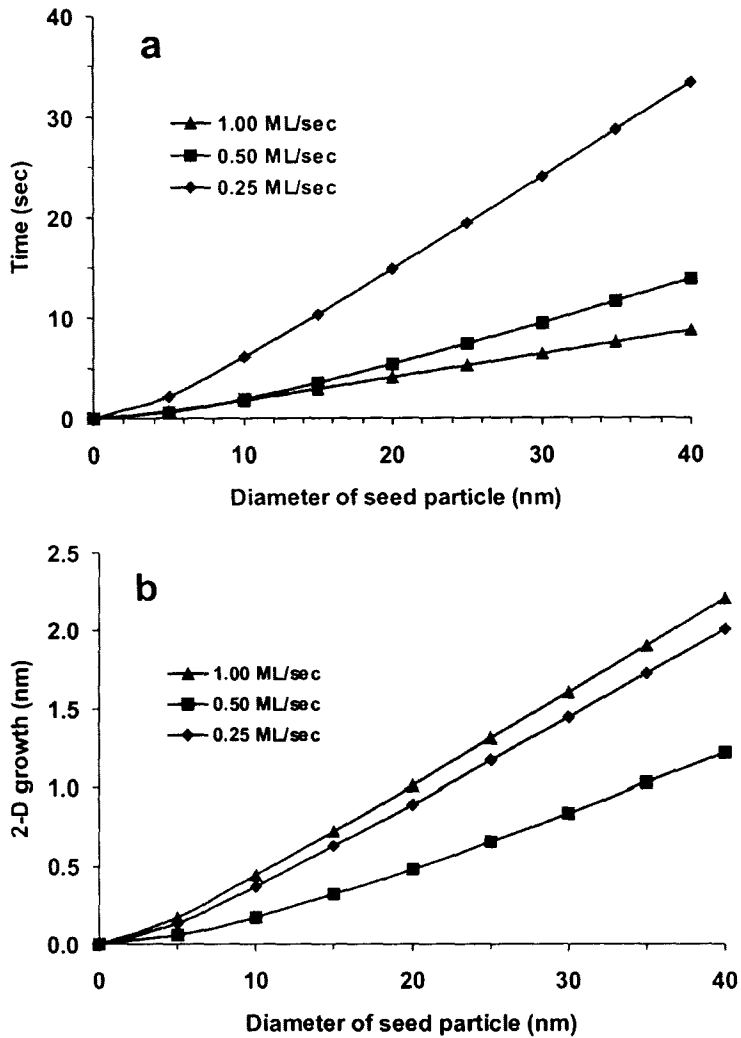
Figure 6.10 (a) Theoretical analysis of size-dependent 'incubation time' of gold seed particles to reach thermodynamic equilibrium with group III material. (b) Thickness of 2-D layer deposited during 'incubation time' as calculated for different sizes of seed particles.

Our analysis shows that the seed particles prior to growth evolving from 1 nm of gold (sample D-F) have an average diameter (<r>) of 17.6 nm and a density ($P_{particle}$) of $8.8 \times 10^{10} / cm^2$. As shown in Figure 6.2, for a deposition rate of 1μm/h (equivalent to 1 ML/sec or a 2-D growth rate of 0.28 nm/sec), 91.0% of deposited atoms have taken part

in the growth of the 2-D layer, whereas 9.0% of the atoms have been incorporated into the growth of nanowires. Similarly, the overall incorporation of adatoms into the 1-D crystal was 37% for a deposition rate of 0.5 μm/h (equivalent to 0.5 ML/sec, or 2-D growth rate of 0.14 nm/sec) and 14% for a growth rate of 0.25 ML/sec. Substituting these values in Equation 6.6 and plotting them provides us the incubation time depending on the growth rate, as shown in Figure 6.10. As the particle size is increased, larger particles will require more incubation time to reach thermodynamic equilibrium at any specific growth rate. Once equilibrium is reached, the particle will supersaturate and nanowires will start to grow.

The nanowire growth rate, as calculated by Dubrovskii *et al.* [107], will also depend on the size of the seed particle. Unless affected by the Gibbs-Thomson effect, for a specific growth rate, smaller nanowires grow faster than the larger ones. This means that, in addition to having longer incubation time, larger diameter nanowires will require more time to reach any specific height. Due to the larger size of Au particles in the pits (Fig. 6.3), <111> oriented nanowires grow more slowly than <011> nanowires. As a result, <111> directed nanowires nucleating from {111}B sidewall facets [44] of the shallow pit, as mentioned in the last chapter (Treatment C), might encounter the 2-D film, become pinned to the substrate surface, and will continue to grow on the substrate as creeping nanowires along <011> directions. This observation agrees with the growth of <011> nanowires on GaAs (100) substrate by MOCVD in which the 2-D growth was encouraged to trigger the growth along the <011> direction [108].

6.3.4 Crystal Structure and Growth Direction

Crystallographic analysis revealed that nanowires of all orientation except vertical (100) nanowires had wurtzite crystal structure with a periodic array of stacking faults perpendicular to the <111> direction. The <100>-oriented nanowire was found to be defect-free with zincblende crystal structure.

<211>-oriented nanowires were found mostly in the dense areas on the substrate. As shown in Figure 6.7(a), the <211> directed nanowires were initiated along a <111>B direction, but the growth was later changed to a <211> direction, perpendicular to the previous direction, making an angle 54.7° with the substrate. In the case of <111> directed nanowires, (111) planes lie perpendicular to the growth direction, and since the <211> directed nanowires grew perpendicular to <111> directed nanowires, they appeared to have {111} planes lying parallel to the growth direction (Figure 6.7(d) and Figure 6.7(e)).

The <511> directed nanowires have been found to make a transition to wurtzite crystal structure coincident with a change in growth direction. It appears that the nanowire started to grow vertically and later changed the growth direction. Analysis of the [100] nanowire showed that it maintains zincblende crystal structure throughout the crystal, which, in essence, supports our observation that the growth of <511> nanowires occurred as a result of a transition from the [100] direction. The change in growth direction could occur due to strain [33], or anisotropy of growth as a result of competition between growth planes. Both <511> and <211> oriented nanowires were found in the dense area on the substrate.

As shown in Figure 6.9, the <100> oriented nanowire was found to be free from defects. The most common defect in zincblende crystal generally occurs in the form of twins along <111> directions [109,110]. Analysis of nanowires along [011] and [012] directions confirmed that no planar defects were found in the nanowire.

6.4 Chapter Summary

Growth of nanowires on GaAs (100) substrates can be controlled by changing the growth rate and the size of seed particles. Increasing the growth rate has the effect of increasing the surface density of nanowires as well as formation of a 2-D layer having a thickness determined by the overall distribution of seed particles prior to growth. The rate of incorporation of adatoms into the 1-D crystal, i.e., the nanowire growth rate, reaches a maximum value at an intermediate growth rate, which appears to be due to the Gibbs-Thomson effect and competition of adatoms to get incorporated into the 2D layer or nanowires. However, this study reveals the pathways of controlling the nanowire orientation on GaAs (100) substrates. To obtain creeping nanowires, growth should take place at higher growth rate with relatively larger seed particle distribution, whereas the abundance of <111> directed nanowires can be significantly increased by increasing the nanowire growth rate with relatively smaller seed particle distribution.

By analyzing the crystallographic properties of <111>, <211>, <511> and <100> nanowires, it has been demonstrated that, except for <100> oriented nanowires, all nanowires have wurtzite crystal structure. The <100> directed nanowire was found to be

free of defects having zincblende crystal structure. Moreover, a possible growth scenario of <211> and <511> nanowires has been proposed based on their crystallographic analyses.

Chapter 7

Conclusions and Future Work

Through the chemical and structural analysis of the seed particle formation process, surface topography, and nanowires, this thesis aimed at exploring the underlying physical and chemical processes with a view to understanding and controlling the orientation of nanowires on GaAs (100) substrates. The major findings of this study can be summarized as follows:

(1)   The UV-ozone oxide consists of Ga_2O_3, $-As_xGa_2O$, $Ga(OH)_3$, As_2O_3, As_2O_5 and elemental As. The UV-ozone oxide layer has a complex physical structure with Ga_2O_3 and elemental As residing close to the substrate while the concentration of $-As_xGa_2O$ increases at the surface with a layer of As_2O_5 on top, and As_2O_3 distributed all through the oxide layer. Annealing UV-ozone oxide at 500 °C for 300 s results in complete desorption of As_2O_5 and $Ga(OH)_3$ and partial desorption of As_2O_3 and Ga_2O making the oxide layer rich in Ga_2O_3. We postulate the

presence of an intermediate oxide $-As_xGa_2O$ based on the atomic arrangement in GaAs crystal lattice. The evolution of As, Ga_2O_3 and also Ga_2O has been explained based on this assumption. It has also been proposed that Ga_2O_3 is not a direct species of the UV-ozonation process; rather it is produced due to reaction between oxides arising from the UV-ozone process or reaction of As_2O_3 with the bulk substrate. Moreover, gallium does not form an alloy with gold nanoparticles fabricated on the oxide layer.

(2)   As part of the seed particle formation process, the role and efficiency of proximity caps have been studied in detail. As described in Chapter 4, the effectiveness of proximity caps depends on the geometry and structure of the sample. GaAs proximity caps used in annealing UV-Ozone oxidized GaAs have the advantage of acting as a sacrificial layer in addition to creating a local overpressure of As that inhibits the loss of arsenic from the sample. In the case of gold coated UV-Ozone oxide, it has been found that the proximity caps play no significant role in annealing the sample at 500 °C. In both cases, deterioration of the GaAs (100) surface has occurred due to the formation of pits and the latter has pits much deeper due to the bulk utilization by the oxide layer. These pits, as revealed by XPS and EDS-HRTEM, consist mostly of Ga_2O_3 with elemental As at the pit oxide interface.

(3)   Both growth direction as well as density of nanowires has been shown to depend on the surface preparation prior to the formation of seed particles. Change in surface preparation not only affects the distribution of seed particle, but also

results in a surface topography that is significantly different from one another. In relation to nanowire growth, it has also been shown that it is possible to change the orientation of nanowires by optimizing the growth rate as well as distribution of seed particles during growth. A simple model has also been proposed to calculate size-dependent 'incubation time' for seed particles, which may play a role in the orientation of nanowires. Moreover, crystallographic analyses of nanowires reveal that the vertical (100) nanowires are nearly defect-free having zincblende crystal structure, whereas nanowires growing along other directions have wurtzite crystal structure with stacking faults.

The thesis notably shows the routes of controlling the orientation of nanowires on GaAs (100) substrates, and we have optimized the conditions of triggering the growth along <111> and <011> directions. Further work is required to trigger the growth along other directions. As a continuation of this work, the following work is proposed:

(1) In order to establish a generic growth model of nanowires on III-V substrates, a systematic study regarding the formation of seed particles as well as growth of nanowires can be carried out on GaAs(111)B substrates as well as (100) substrates of a different III-V material (such as InP). However, for better understanding of the physical processes involved during nanowire growth, it is required to ensure a uniform distribution of monodisperse seed particles on the substrate. Use of block copolymers could be a promising option.

(2) In this thesis, orientation-dependence of nanowires has been studied at a fixed temperature of 500 °C for different growth rates. The effect of temperature as well as growth rate on the orientation of nanowires could be studied in order to establish an in-depth understanding of nanowire growth on GaAs (100) substrates.

(3) Growing defect-free [100] oriented nanowires on (100) substrates is the key challenge to researchers at present. We observed an increase in the surface density (from 1.9% to 7.0%) of [100] oriented nanowires when the growth rate was lowered from 1.0 ML/sec to 0.50 ML/sec (for example sample D vs. E of Chapter 6.0). It is required, though, to explore the growth mechanism of these nanowires and hence, to optimize the growth conditions accordingly with a view to triggering the growth along [100] direction.

References

[1] Y. Cui, Q. Wei, H. Park, and C. M. Lieber, Science **293**, 1289 (2001).

[2] G. Zheng, F. Patolsky, Y. Cui, W. U. Wang, and C. M. Lieber, Nat. Biotechnol. **23**, 1294 (2005).

[3] B. Tian, X. Zheng, T. J. Kempa, Y. Fang, N. Yu, G. Yu, J. Huang, and C. M. Lieber, Nature **449**, 885 (2007).

[4] M. Law, L. E. Greene, J. C. Johnson, R. Saykally, and P. Yang, Nat. Mater. **4**, 455 (2005).

[5] E. Tutuc, J. Appenzeller, M. C. Reuter, and S. Guha, Nano Lett. **6**, 2070 (2006).

[6] Y. Li, F. Qian, J. Xiang, and C. M. Lieber, Materials Today **9**, 18 (2006).

[7] J. Goldberger, A. I. Hochbaum, R. Fan, and P. Yang, Nano Lett. **6**, 973 (2006).

[8] J. Bao, M. A. Zimmler, F. Capasso, X. Wang, and Z. F. Ren, Nano Lett. **6**, 1719 (2006).

[9] X. Duan, Y. Huang, Y. Cui, J. Wang, and C. M. Lieber, Nature **409**, 66 (2001).

[10] X. Duan, Y. Huang, R. Agarwal, and C. M. Lieber, Nature **421**, 241 (2003).

[11] A. I. Boukai, Y. Bunimovich, J. Tahir-Kheli, J. Yu, I. Goddard William A., and J. R. Heath, Nature **451**, 168 (2008).

[12] A. I. Hochbaum, R. Chen, R. D. Delgado, W. Liang, E. C. Garnett, M. Najarian, A. Majumdar, and P. Yang, Nature **451**, 163 (2008).

[13] N. Wang, Y. Cai, and R. Q. Zhang, Mat. Sci. Eng.: R: Reports, **60**, 1 (2008).

[14] R. S. Wagner and W. C. Ellis, Appl. Phys. Lett. **4**, 89 (1964).

[15] E. I. Givargizov, J. Cryst. Growth **31**, 20 (1975).

[16] K. Hiruma, T. Katsuyama, K. Ogawa, M. Koguchi, H. Kakibayashi, and G. P. Morgan, Appl. Phys. Lett. **59**, 431 (1991).

[17] K. Hiruma, M. Yazawa, T. Katsuyama, K. Ogawa, K. Haraguchi, M. Koguchi, and H. Kakibayashi, J. Appl. Phys. **77**, 447 (1995).

[18] R. S. Wagner, *VLS mechanism of crystal growth* (Wiley-Interscience, New York, 1970), p. 47.

[19] J. W. Niemantsverdriet and I. Chorkendorff, *Concepts of modern catalysis and kinetics* (Wiley-VCH, 2003).

[20] M. Borgström, K. Deppert, L. Samuelson, and W. Seifert, J. Cryst. Growth **260**, 18 (2004).

[21] P. Paiano, P. Prete, N. Lovergine, and A. M. Mancini, J. Appl. Phys. **100**, 094305 (2006).

[22] D. H. Reep and S. K. Ghandhi, J. Electrochem. Soc. **130**, 675 (1983).

[23] M. A. Verheijen, G. Immink, T. de Smet, M. T. Borgstrom, and E. P. A. M. Bakkers, J. Am. Chem. Soc. **128**, 1353 (2006).

[24] S. Kodambaka, J. Tersoff, M. C. Reuter, and F. M. Ross, Science **316**, 729 (2007).

[25] J. Johansson, B. A. Wacaser, K. A. Dick, and W. Seifert, Nanotechnology **17**, S355 (2006).

[26] H. Tuan, D. C. Lee, T. Hanrath, and B. A. Korgel, Nano Lett. **5**, 681 (2005).

[27] Y. Yao and S. Fan, Mater. Lett. **61**, 177 (2007).

[28] J. Arbiol, B. Kalache, P. R.I. Cabarrocas, J. R. Morante, and A. F. i. Morral, Nanotechnology **18**, 305606 (2007).

[29] Y. Wang, V. Schmidt, S. Senz, and U. Gosele, Nat. Nano. **1**, 186 (2006).

[30] I. Regolin, V. Khorenko, W. Prost, F. J. Tegude, D. Sudfeld, J. Kastner, G. Dumpich, K. Hitzbleck, and H. Wiggers, J. Appl. Phys. **101**, 054318 (2007).

[31] K. A. Dick, Progress in Crystal Growth and Characterization of Materials **54**, 138 (2008).

[32] T. Martensson, C. P. T. Svensson, B. A. Wacaser, M. W. Larsson, W. Seifert, K. Deppert, A. Gustafsson, L. R. Wallenberg, and L. Samuelson, Nano Lett. **4**, 1987 (2004).

[33] Z. H. Wu, X. Mei, D. Kim, M. Blumin, H. E. Ruda, J. Q. Liu, and K. L. Kavanagh, Appl. Phys. Lett. **83**, 3368 (2003).

[34] U. Krishnamachari, M. Borgstrom, B. J. Ohlsson, N. Panev, L. Samuelson, W. Seifert, M. W. Larsson, and L. R. Wallenberg, Appl. Phys. Lett. **85**, 2077 (2004).

[35] M. C. Plante and R. R. LaPierre, Nanotechnology **19**, 495603 (2008).

[36] H. Shtrikman, R. Popovitz-Biro, A. Kretinin, L. Houben, M. Heiblum, M. Bukala, M. Galicka, R. Buczko, and P. Kacman, Nano Lett. **9**, 1506 (2009).

[37] Y. Cai, S. &. Chan, K., I. &. Sou, K., Y. &. Chan, F., D. &. Su, S., and N. Wang, Adv Mater **18**, 109 (2006).

[38] V. Schmidt, S. Senz, and U. Gosele, Nano Lett. **5**, 931 (2005).

[39] W. Braun, V. M. Kaganer, A. Trampert, H. Schönherr, Q. Gong, R. Nötzel, L. Däweritz, and K. H. Ploog, J. Cryst. Growth **227-228**, 51 (2001).

[40] Y. Wu, Y. Cui, L. Huynh, C. J. Barrelet, D. C. Bell, and C. M. Lieber, Nano Lett. **4**, 433 (2004).

[41] M. C. Plante, J. Garrett, S. C. Ghosh, P. Kruse, H. Schriemer, T. Hall, and R. R. LaPierre, Appl. Surf. Sci. **253**, 2348 (2006).

[42] S. C. Ghosh, M. C. Biesinger, R. R. Lapierre, and P. Kruse, J. Appl. Phys. **101**, 114322 (2007).

[43] S. C. Ghosh, M. C. Biesinger, R. R. Lapierre, and P. Kruse, J. Appl. Phys. **101**, 114321 (2007).

[44] S. C. Ghosh, P. Kruse, and R. R. LaPierre, Nanotechnology **20**, 115602 (2009).

[45] S. Bhunia, T. Kawamura, Y. Watanabe, S. Fujikawa, and K. Tokushima, Appl. Phys. Lett. **83**, 3371 (2003).

[46] A. I. Hochbaum, R. Fan, R. He, and P. Yang, Nano Lett. **5**, 457 (2005).

[47] T. Martensson, M. Borgstrom, W. Seifert, B. J. Ohlsson, and L. Samuelson, Nanotechnology **14**, 1255 (2003).

[48] Z. H. Wu, X. Y. Mei, D. Kim, M. Blumin, and H. E. Ruda, Appl. Phys. Lett. **81**, 5177 (2002).

[49] M.R. H. Nezhad, R., M. Aizawa, L. A. Porter, A. E. Ribbe and E. J. Buriak, Small **1**, 1076 (2005).

[50] K. A. Dick, K. Deppert, T. Martensson, W. Seifert, and L. Samuelson, J. Cryst. Growth **272**, 131 (2004).

[51] Y. C. Kang and S. B. Park, J. Aerosol Sci. **26**, 1131 (1995).

[52] S. Ingrey, J. Vac. Sci. Technol. A **10**, 829 (1992).

[53] Z. Lu, M. T. Schmidt, D. V. Podlesnik, C. F. Yu, and J. Osgood R.M., J. Chem. Phys. **93**, 7951 (1990).

[54] S. I. Yi, P. Kruse, M. Hale, and A. C. Kummel, J. Chem. Phys. **114**, 3215 (2001).

[55] J. Z. Sexton, S. I. Yi, M. Hale, P. Kruse, A. A. Demkov, and A. C. Kummel, J. Chem. Phys. **119**, 9191 (2003).

[56] P. Kruse, J. G. McLean, and A. C. Kummel, J. Chem. Phys. **113**, 9224 (2000).

[57] P. Kruse, J. G. McLean, and A. C. Kummel, J. Chem. Phys. **113**, 9217 (2000).

[58] A. S. Jordan and A. Robertson, J. Vac. Sci. Technol. A **12**, 204 (1994).

[59] T. Van Buuren, M. K. Weilmeier, I. Athwal, K. M. Colbow, J. A. Mackenzie, T. Tiedje, P. C. Wong, and K. A. R. Mitchell, Appl. Phys. Lett. **59**, 464 (1991).

[60] M. Adamcyk, T. Pinnington, A. Ballestad, and T. Tiedje, Mat. Sci. Eng. B **75**, 153 (2000).

[61] S. Ritchie, S. R. Johnson, C. Lavoie, J. A. Mackenzie, T. Tiedje, and R. Streater, Surf Sci **374**, 418 (1997).

[62] M. C. Plante, *Metal-Assisted Growth of III-V Nanowires by MBE* (Ph.D. thesis, McMaster University, Hamilton, Ontario, 2009).

[63] R. F. Egerton and M. Malac, Journal of Electron Spectroscopy and Related Phenomena **143**, 43 (2005).

[64] R. D. Leapman and J. A. Hunt, Microsc.Microanal.Microstruct. **2**, 231 (1991).

[65] R. D. Leapman and D. E. Newbury, Anal. Chem. **65**, 2409 (1993).

[66] Z. H. Lu, B. Bryskiewicz, J. McCaffrey, Z. Wasilewski, and M. J. Graham, J. Vac. Sci. Technol. B **11**, 2033 (1993).

[67] http://srdata.nist.gov/xps

[68] E. A. Albanesi, S. J. Sferco, I. Lefebvere, G. Allan, and G. Hollinger, Phys. Rev. B **46**, 13260 (1992).

[69] G. P. Schwartz, G. J. Gualtieri, G. W. Kammlott, and B. Schwartz, J. Electrochem. Soc. **126**, 1737 (1979).

[70] C. C. Surdu-Bob, S. O. Saied, and J. L. Sullivan, Appl. Surf. Sci. **183**, 126 (2001).

[71] J. Massies and J. P. Contour, J. Appl. Phys. **58**, 806 (1985).

[72] R. P. Vasquez, B. F. Lewis, and F. J. Grunthaner, Appl. Phys. Lett. **42**, 293 (1983).

[73] J. T. Wolan, C. K. Mount, and G. B. Hoflund, Appl. Phys. Lett. **72**, 1469 (1998).

[74] E. S. Aydil, K. P. Giapis, R. A. Gottscho, V. M. Donnelly, and E. Yoon, J. Vac. Sci. Technol. B **11**, 195 (1993).

[75] J. Shin, K. M. Geib, C. W. Wilmsen, P. Chu, and H. H. Wieder, J. Vac. Sci. Technol. A **9**, 1029 (1991).

[76] M. Beerbom, O. Henrion, A. Klein, T. Mayer, and W. Jaegermann, Electrochim. Acta **45**, 4663 (2000).

[77] G. Hollinger, R. Skheyta-Kabbani, and M. Gendry, Physical Review B (Condensed Matter) **49**, 11159 (1994).

[78] Z. Lu, M. T. Schmidt, D. Chen, J. Osgood R.M., W. M. Holber, D. V. Podlesnik, and J. Forster, Appl. Phys. Lett. **58**, 1143 (1991).

[79] M. Schäfer, W. Naumann, T. Finnberg, M. Hannss, A. Dutschke, and R. Anton, Appl. Surf. Sci. **158**, 147 (2000).

[80] D. R. Lide, *CRC handbook of chemistry and physics* (CRC press, Boca Raton, FL, 1994).

[81] S. Ingrey, W. M. Lau, and N. S. McIntyre, J. Vac. Sci. Technol. A **4**, 984 (1986).

[82] T. Ishikawa and H. Ikoma, Jpn. J. App. Phys. **31**, 3981 (1992).

[83] K. Tone, M. Yamada, Y. Ide, and Y. Katayama, Jpn. J. App. Phys. **31**, 721 (1992).

[84] D. A. Allwood, S. Cox, N. J. Mason, R. Palmer, R. Young, and P. J. Walker, Thin Solid Films **412**, 76 (2002).

[85] H. N. Aiyer, V. Vijayakrishnan, G. N. Subbanna, and C. N. R. Rao, Surf Sci **313**, 392 (1994).

[86] M. Passlack, J. K. Abrokwah, Z. Yu, R. Droopad, C. Overgaard, and H. Kawayoshi, Appl. Phys. Lett. **82**, 1691 (2003).

[87] M. H. Badawi and J. Mun, Electronics Letters **20**, 125 (1984).

[88] H. Kohzu, M. Kuzuhara, and Y. Takayama, J. Appl. Phys. **54**, 4998 (1983).

[89] G. W. Smith, A. J. Pidduck, C. R. Whitehouse, J. L. Glasper, and J. Spowart, J. Cryst. Growth **127**, 966 (1993).

[90] G. W. Smith, A. J. Pidduck, C. R. Whitehouse, J. L. Glasper, A. M. Keir, and C. Pickering, Appl. Phys. Lett. **59**, 3282 (1991).

[91] M. Yamada and Y. Ide, Surface Science **339**, L914 (1995).

[92] V. G. Weizer and N. S. Fatemi, J. Appl. Phys. **64**, 4618 (1988).

[93] A. Guillén-Cervantes, Z. Rivera-Alvarez, M. López-López, E. López-Luna, and I. Hernández-Calderón, Thin Solid Films, **373**, 159 (2000).

[94] A. C. Warren, J. M. Woodall, J. L. Freeouf, D. Grischkowsky, D. T. McInturff, M. R. Melloch, and N. Otsuka, Appl. Phys. Lett. **57**, 1331 (1990).

[95] W. G. Moffatt and General Electric Company. Business Growth Services, *Handbook of binary phase diagrams.* -- (General Electric Co., Corporate Research and Development, Business Growth Services, Schenectady, N.Y., 1976).

[96] J. A. Venables, L. Giordano, and J. H. Harding, J. Phys. cond. mat. **18**, 411 (2006).

[97] C. Ratsch and J. A. Venables, J. Vac. Sci. Tech. A: Vacuum, Surfaces and Films **21**, 96 (2003).

[98] Z. Chen and C. Cao, Appl. Phys. Lett. **88**, 143118 (2006).

[99] T. Y. Tan, N. Li, and U. Gösele, Appl Phys A **78**, 519 (2004).

[100] A. Kley, P. Ruggerone, and M. Scheffler, Phys. Rev. Lett. **79**, 5278 (1997).

[101] F. Glas, J. Harmand, and G. Patriarche, Phys. Rev. Lett. **99**, 146101 (2007).

[102] M. I. McMahon and R. J. Nelmes, Phys. Rev. Lett. **95**, 215505 (2005).

[103] N. V. Sibirsev, V. G. Dubrovskii, G. E. Cirlin, V. A. Egorov, Y. B. Samsonenko, and V. M. Ustinov, Semiconductors **42**, 1259 (2008).

[104] X. Shen, D. Kishimoto, and T. Nishinaga, Jpn. J. App. Phys. **33**, 11 (1994).

[105] C. Soci, X. Bao, D. P. R. Aplin, and D. Wang, Nano Lett. **8**, 4275 (2008).

[106] V. G. Dubrovskii, N. V. Sibirev, G. E. Cirlin, J. C. Harmand, and V. M. Ustinov, Phys Rev E. **73**, 021603 (2006).

[107] V. G. Dubrovskii and N. V. Sibirev, J. Cryst. Growth **304**, 504 (2007).

[108] S. A. Fortuna, J. Wen, I. S. Chun, and X. Li, Nano Lett. **8**, 4421 (2008).

[109] S. D. Hersee, X. Sun, and X. Wang, Nano Lett. **6**, 1808 (2006).

[110] M. A. Herman, W. Richter, and H. Sitter, *Epitaxy - Physical Princinples and Technical Implementation* (Springer-Verlag Berlin Heidelberg, Germany, 2004).